A new mechanism of fibronectin fibril assembly revealed by live imaging and super-resolution microscopy.

Darshika Tomer[1], Cecilia Arriagada[1], Sudipto Munshi[2,‡], Brianna E. Alexander[1,3], Brenda French[2], Pavan Vedula[4], Valentina Caorsi[5], Andrew House[6], Murat Guvendiren[6], Anna Kashina[4], Jean E. Schwarzbauer[7], and Sophie Astrof[1,*].

1. Department of Cell Biology and Molecular Medicine, Cardiovascular Research Institute, Rutgers Biomedical and Health Sciences, 185 South Orange Ave, Newark, NJ, 07103, USA.

2. Sidney Kimmel Medical College of Thomas Jefferson University, Philadelphia, PA, 19107, USA

3. Multidisciplinary Ph.D. Program in Biomedical Sciences. Cell Biology, Neuroscience and Physiology track, Rutgers Biomedical and Health Sciences, Newark, NJ, 07103, USA.

4. Department of Biomedical Sciences, University of Pennsylvania, Philadelphia, PA 19104, USA

5. Abbelight, 191 Avenue Aristide Briand, 94230 Cachan, France

6. Otto H. York Chemical and Materials Engineering, Department of Biomedical Engineering, New Jersey Institute of Technology, Newark, NJ 07102, USA

7. Department of Molecular Biology, Princeton University, Princeton, New Jersey, USA

‡Current Address: Department of Chemical and Structural Biology, Weizmann Institute of Science, Rehovot, Israel

*Author for correspondence: Sophie Astrof, Ph.D.

Phone: 617-429-8295

E-mail: sophie.astrof@rutgers.edu

Abstract

- Fn1 fibrils have long been viewed as continuous fibers composed of extended, periodically aligned Fn1 molecules. However, our live imaging and single-molecule localization microscopy (SMLM) are inconsistent with this traditional view and show that Fn1 fibrils are composed of roughly spherical nanodomains containing 6-11 Fn1 dimers. As they move toward the cell center, Fn1 nanodomains become organized into linear arrays, wherein nanodomains are spaced at the average periodicity of 105±17 nm. Periodical Fn1 nanodomain arrays are bona fide fibrils: they are resistant to deoxycholate treatment and retain nanodomain periodicity in the absence of cells. The nanodomain periodicity in fibrils remained constant when probed with antibodies recognizing distinct Fn1 epitopes or combinations of antibodies recognizing epitopes spanning the length of Fn1. FUD, a bacterial peptide that binds Fn1 N-terminus and disrupts Fn1 fibrillogenesis does not disrupt the formation of Fn1 nanodomains, instead, it blocks the organization of Fn1 nanodomains into periodical arrays. These studies establish a new paradigm of Fn1 fibrillogenesis.

Introduction

Fibronectin (Fn1) is a requisite component of the extracellular matrix (ECM) necessary for embryogenesis and homeostasis (Schwarzbauer and DeSimone, 2011). In the absence of Fn1 fibrillogenesis, the binding of Fn1 to cells is not sufficient to regulate key biological processes such as embryonic development, angiogenesis, vascular remodeling, or cartilage condensation (Chiang et al., 2009; Rozario et al., 2009; Singh and Schwarzbauer, 2014; Zhou et al., 2008). Therefore, understanding the mechanisms by which Fn1 proteins assemble into macromolecular fibrils is essential to gain insights into the various functions of Fn1. Fn1 is secreted as a dimer wherein two Fn1 molecules are held in an anti-parallel orientation by two disulfide bonds close to their C-termini (Skorstengaard et al., 1986; Wagner and Hynes, 1979). Fn1 fibrillogenesis is a cell-dependent process (McKeown-Longo and Mosher, 1983), occurs following the binding of Fn1 dimers to cell-surface integrins (Schwarzbauer and DeSimone, 2011). Following integrin binding, intracellular cytoskeletal forces such as actomyosin contractility acting through integrins generate pulling forces on Fn1 dimers, exposing epitopes that promote Fn1 fibrillogenesis (Chernousov et al., 1987; Hocking et al., 1994; Smith et al., 2007; Zhang et al., 1994; Zhang et al., 1997; Zhong et al., 1998). At a cellular level, the process of Fn1 fibrillogenesis is correlated with the formation of fibrillar adhesions, whereby small mobile adhesions containing Fn1 and integrin $\alpha5\beta1$ somehow elongate while translocating toward the nucleus, first giving rise to focal adhesions (< 1 μm), and then as the translocation continues, to longer filaments, termed fibrillar adhesions ($\geq$1 μm) containing Fn1 and intracellular cytoplasmic effectors linking Fn1 and actin cytoskeleton (Geiger et al., 2001; Geiger and Yamada, 2011; Lu et al., 2020; Pankov et al., 2000; Zamir et al., 1999; Zamir et al., 2000).

It has been thought that Fn1 fibrils resemble ropes, in which extended Fn1 dimers align such that regions containing overlapping N-termini alternate with regions containing C-termini

73 (Chen et al., 1997; Dzamba and Peters, 1991; Fruh et al., 2015), also illustrated in **Sup. Fig.**
74 **8A**. To understand how the process of fibrillogenesis occurs in real-time and at a nanoscale
75 level, we adopted a CRISPR/Cas9-mediated mutagenesis approach to generate fluorescently-
76 labeled Fn1, which was subject to the physiological regulation of expression and splicing. This
77 approach has enabled visualization of Fn1 fibrillogenesis over an extended time. Using live
78 imaging and super-resolution microscopy, we uncovered an unexpected mechanism of Fn1
79 fibrillogenesis.

80 Our data demonstrate that Fn1 fibrils form as a result of centripetally-moving Fn1
81 nanodomains originating at the cell periphery. As Fn1 nanodomains move toward the cell
82 center, they assemble into arrays of periodically-spaced nanodomains. The arrays become
83 longer as the movement towards the cell center continues and as more nanodomains are
84 added. We show that these nanodomain arrays are in bona fide fibrils and that each Fn1
85 nanodomain contains multiple Fn1 dimers. Our live imaging and SMLM reveal a new role by
86 which the N-terminal region of Fn1 protein regulates fibril assembly, and show that interactions
87 mediated by the N-terminal Fn1 assembly region are not required for the formation of Fn1
88 nanodomains or their centripetal translocation; Instead, the N-terminus of Fn1 regulates the
89 organization of Fn1 nanodomains into nanodomain arrays. Our model integrates the process
90 of fibrillogenesis with the process of adhesion elongation and provides significant new insights
91 into the mechanisms of Fn1 ECM formation, remodeling, and signaling.

92

93 **Results**

94 **Beaded structure of Fn1 fibrils revealed by diffraction-limited microscopy**

95 While examining $Fn1^{+}$ ECM in mid-gestation mouse embryos by confocal
96 immunofluorescence microscopy using an Abcam monoclonal anti-Fn1 antibody which binds
97 an epitope within a central region of Fn1 (**Table M2** in Methods), we observed that Fn1 fibrils
98 in the pharyngeal arches and the heart appeared dotted, with regularly-spaced regions of high

99 and low fluorescence intensity (**Fig. 1, Movie 1**). The dotted appearance of embryonic Fn1
100 suggested that the distribution of Fn1 molecules in Fn1 fibrils is not homogenous. To
101 understand how Fn1 fibrils form, we employed a CRISPR/Cas9 knock-in strategy to modify the
102 endogenous Fn1 locus by replacing the termination codon of Fn1 with a sequence encoding a
103 fluorescent protein. We used this strategy to generate cell lines and Fn1$^{mEGFP/mEGFP}$
104 homozygous knock-in mice expressing Fn1 fused to monomeric enhanced green fluorescent
105 protein (mEGFP) or other monomeric fluorescent proteins (**Sup. Figs. 1-2**). Homozygous
106 Fn1$^{mEGFP/mEGFP}$ mice were obtained at the correct Mendelian ratio (**Sup. Fig. 1B,** panels 4 and
107 5), and are viable and fertile, indicating that Fn1-mEGFP supports all functions of Fn1
108 necessary for embryonic development, fetal viability, and adult homeostasis. Examination of
109 Fn1 expression patterns in knock-in mice showed that Fn1-mEGFP is expressed in the same
110 pattern as the unmodified Fn1 in embryos (Peters and Hynes, 1996), i.e., there were no
111 regions that were GFP+ but Fn1-negative and vice versa in Fn1$^{mEGFP/+}$ embryos expressing
112 one wild-type allele of Fn1 (**Sup. Fig. 2D**). In addition, we used CRISPR/Cas9 mutagenesis to
113 generate five independent lines of mouse embryo fibroblasts (MEFs) expressing Fn1-mEGFP,
114 Fn1-mScarlet-I, Fn1-Neon Green, or Fn1-tdTomato fluorescent proteins (FP). Western blots
115 showed that FP fusions to Fn1 were specific: FPs were only fused to Fn1 as no other FP
116 fusions were detected either by western blotting or immunofluorescence (IF) (**Sup. Fig. 2A-B**).
117 Measuring deoxycholate (DOC) insolubility of Fn1 ECM is a classical biochemical assay
118 to assay stable incorporation Fn1 proteins into the ECM (Choi and Hynes, 1979; McKeown-
119 Longo and Mosher, 1983; Schwarzbauer, 1991; Singh et al., 2010; Wierzbicka-Patynowski et
120 al., 2004). For these assays, we carefully controlled the number of cells plated, as cell density
121 affects the extent of Fn1 fibrillogenesis (Hynes, 1990). We performed DOC insolubility assays
122 using 5 independently-generated cells lines expressing Fn1-FP proteins. These experiments
123 demonstrated that the incorporation of Fn1-FPs into the ECM was indistinguishable from wild-
124 type, untagged Fn1 (**Sup. Fig. 2C**). Together with the viability of Fn1$^{mEGFP/mEGFP}$ homozygous

125 knock-in mice, these data demonstrate that Fn1-FP fusion proteins are suitable reagents for
126 investigating mechanisms of Fn1 fibrillogenesis.

127 To visualize the process of fibrillogenesis in real-time, we plated Fn1$^{mEGFP/+}$ MEFs on
128 the gelatin-coated cover glass and imaged cells 16 hours after plating using total internal
129 reflection (TIRF) microscopy at the critical angle of incidence. These experiments showed that
130 Fn1 fibrillogenesis initiated at cell periphery as distinct, brightly-fluorescent Fn1 densities that
131 moved centripetally in parallel with F-actin and became aligned into linear arrays of "beads"
132 (arrows in **Movie 2**). TIRF imaging also showed that domains of higher fluorescence intensity
133 of Fn1 co-localized with integrin $\alpha5\beta1$ both in non-fibrillar (arrows in **Fig. 2A-A2**) and in fibrillar
134 adhesions (arrows in **Fig. 2B-B2**), and that both Fn1 and $\alpha5\beta1$ fibrillar adhesions appeared
135 beaded (**Fig. 2B-B2**, arrows). Beaded architecture of Fn1 fibrils was also observed by an
136 independent imaging method using Zeiss Airyscan technology (**Sup. Fig. 3**). To test whether
137 the beaded appearance of Fn1 fibrils depended on antibody epitope availability, we stained
138 wild-type MEFs or mouse endothelial cells using three different antibodies 1) 297.1 polyclonal
139 antibody raised against the rat plasma Fn1 protein and recognizing multiple Fn1 epitopes
140 (**Sup. Fig. 4)**; 2) 3E2 monoclonal antibody recognizing the alternatively spliced EIIIA exon of
141 Fn1, and 3) an Abcam monoclonal antibody recognizing an epitope within the central region of
142 Fn1 (see **Table M2**, in Methods). The beaded appearance of Fn1 fibrils did not depend on the
143 type of antibody used (**Sup. Fig. 5**). Moreover, staining with a polyclonal antibody to Fn1,
144 297.1, which recognizes multiple epitopes along the Fn1 molecule resulted in the beaded
145 appearance of Fn1 fibrils (**Sup. Fig. 5A-A1**). Fn1 fibrils formed by cells plated on uncoated
146 glass, as well as on glass coated with gelatin, laminin 111, or vitronectin, also appeared
147 beaded **Sup. Figs. 5-6**). Similarly, Fn1 fibrils in cell-free areas (**Sup. Fig. 5A, A1**) and between
148 cells were beaded (**Sup Fig. 5B, B1, C, C1**). Fn1 fibrils produced by cells plated on soft
149 substrata such as hydrogels of variable stiffness also appeared beaded (**Sup. Fig. 6C-D, 6C1-**

150 **D1**). In this latter experiment, Fn1 was detected by imaging the fluorescence of Fn1-mEGFP
151 protein, indicating that the beaded appearance of Fn1 fibrils is independent of antibody
152 staining. To determine whether Fn1 fibrils in cell-free, fibrillar ECM were beaded, cultures were
153 treated with 2% DOC (Lu et al., 2020). 2% DOC treatment dissolves cell membranes and
154 cytoplasmic components, leaving behind ECM devoid of cell contact (**Movie 3** for time-lapse of
155 dissolution of cellular components, F-actin and DNA). This experiment showed that Fn1 fibrils
156 retained their beaded architecture in the absence of cell contact (**Sup. Fig. 5D**). Taken
157 together, these studies indicated that the beaded appearance of Fn1 fibrils is a general feature
158 of Fn1 ECM that can be seen in multiple contexts: in DOC-resistant cell-free fibrils, in different
159 embryonic tissues *in vivo*, and when cells are cultured on various substrata *in vitro*. Moreover,
160 the beaded appearance of Fn1 fibrils is independent of the type of antibody and a method of
161 detection: It is seen by indirect detection methods such as immunofluorescence and by direct
162 detection of fluorescent Fn1-mEGFP protein.
163

164 **Nanoarchitecture of Fn1 fibrils revealed by standardized single-molecule localization**
165 **microscopy.**

166 To examine the structure of Fn1 fibrils at a nanoscale level, we adopted single-molecule
167 localization microscopy (SMLM) using the direct stochastic optical reconstruction microscopy
168 (dSTORM) method (Heilemann et al., 2008; Rust et al., 2006). To optimize SMLM imaging
169 conditions and determine the effective labeling efficiency of our reagents, we used the
170 methodology and the reference cell line NUP96-mEGFP, as gold-standard tools to optimize
171 image quality, measure effective labeling efficiency, and to quantify the number of GFP
172 molecules in our structure(s) of interest (Lelek et al., 2021; Thevathasan et al., 2019). In this
173 reference cell line, both copies of the *NUP96* gene are modified by CRISPR/Cas9
174 mutagenesis to generate NUP96-mEGFP protein, a component of the nuclear pore complex,
175 NPC (Thevathasan et al., 2019). Thirty-two copies of NUP96 protein are evenly distributed

among the eight corners of the NPC at known distances (see schematic in **Sup. Fig. 7**) (Bui et al., 2013; Thevathasan et al., 2019; von Appen et al., 2015). To optimize our SMLM imaging, we were guided by the current best SMLM practices (Lelek et al., 2021; Mund and Ries, 2020), the methodology, and the SMAP software developed by (Diekmann et al., 2020; Ries, 2020; Thevathasan et al., 2019). Measurements using the Fourier ring correlation method (Nieuwenhuizen et al., 2013) implemented in the SMAP software indicated that the resolution of our images ranged between 14 and 28 nm. Localization precision was 9.1±1.9 nm, on average. Using antibodies to detect NUP96-mEGFP and the SMAP software, we analyzed images from 3 independent experiments, 8 nuclei and 4571 NPCs, and determined the NPC radius to be 63.6±0.86 nm (**Fig. 3A-C** and **Table 1**). This radius is consistent with the reported NPC radius of 64.3+/-2.6 nm, measured using this cell line and a combination of commercial anti-GFP primary and Alexa-647-conjugated secondary antibodies (Thevathasan et al., 2019). We then used NUP96-mEGFP cells to optimize the effective labeling efficiency (ELE) of our reagents. ELE summarily measures how well one's reagents and methods, including the SMLM imaging protocol, generate images that reflect the actual structure under the study (Thevathasan et al., 2019). SMLM imaging of NUP96 in the x-y plane should produce 8-fold symmetrical ring-like structures wherein 4 copies of the NUP96 protein are positioned at each of the NPC's 8 vertices at known intervals and with known dimensions (Thevathasan et al., 2019). Using NUP96-mEGFP as a reference cell line, anti-GFP primary antibodies, commercially-labeled Alexa-647-conjugated secondary antibodies, and the SMAP software (Thevathasan et al., 2019), we analyzed 4,571 NPCs from 8 cells and 3 independent experiments, and determined the ELE to be 79.6±5.4% (**Table 1**), reflecting that the majority of NPCs have eight $NUP96^{+}$ corners in our images (**Fig. 3A-C**). This ELE and the standard deviation of our measurements (<10%) are comparable with the best ELE measured for this system ~74% (Thevathasan et al., 2019). Together, these experiments indicate that our

201 reagents and SMLM imaging conditions are within the accepted SMLM standards (Lelek et al.,
202 2021).

203 To attain a comparable ELE to that measured with NUP96-mEGFP, we stained
204 homozygous Fn1$^{mEGFP/mEGFP}$ MEFs at the same time as NUP96-mEGFP cells, using aliquots of
205 the same mixtures of reagents. Furthermore, pairs of stained Fn1$^{mEGFP/mEGFP}$ MEFs and
206 NUP96-mEGFP cells were imaged on the same day, using aliquots of the same imaging
207 buffer, and the same off-switching and imaging protocols (see Methods). Similar to (Fruh et al.,
208 2015), we saw that Fn1 fibrils appeared as arrays of nanodomains situated along Fn1 fibrils
209 with a regular periodicity (**Figs. 3D-F, Fig. 5D-D2, Fig. 6D-D"**). As in (Fruh et al., 2015),
210 nanodomain periodicity was ascertained using autocorrelation, wherein the position of the first
211 autocorrelated peak marks the nanodomain periodicity (see discussion and simulations in
212 (Fruh et al., 2015)). Autocorrelation analysis of 14 fibrils from 7 cells and 3 independent
213 experiments indicated that the nanodomain periodicity of the GFP epitopes in Fn1-mEGFP
214 fibrils was 102±29 nm (**Figs. 6D-D", 6F, Table 2**). This periodicity is comparable to the
215 nanodomain periodicity measured by (Fruh et al., 2015), which was 99±17 nm, and the
216 periodicity determined by immuno-electron microscopy using anti-EIIIA antibody, which was on
217 average 84 nm and ranged between 40 and 280 nm (Dzamba and Peters, 1991).
218

219 **Localization of Fn1 epitopes within periodical nanodomain arrays**

220 Fn1 is a large, multi-domain, ~250 kDa glycoprotein secreted as a dimer, wherein two
221 Fn1 subunits are linked in an anti-parallel orientation by two di-sulfide bonds at their C-termini
222 (**Fig. 4A**), (Schwarzbauer and DeSimone, 2011; Skorstengaard et al., 1986; Wagner and
223 Hynes, 1979). To investigate the relationship between the protein domains of Fn1 and the
224 nanodomain architecture of Fn1 fibrils, we first used antibodies to different regions of Fn1
225 protein (**Figs. 4B** and **Table M2**). For these experiments, Fn1$^{mEGFP/mEGFP}$ MEFs were plated on
226 uncoated glass coverslips. Cells were then fixed and stained with antibodies recognizing

227 different Fn1 epitopes: 1) R457 rabbit polyclonal antibodies raised to the N-terminal 70 kDa
228 domain of Fn1 (Aguirre et al., 1994; Sechler et al., 2001), 2) R184 rabbit polyclonal antibodies
229 raised to recognize the domain immediately following the 70 kDa N-terminal domain and
230 containing the first six type III repeats of Fn1 (Fn1 III_{1-6}) (Raitman et al., 2018), 3) a rabbit
231 monoclonal antibody from Abcam recognizing an epitope within the central region of Fn1
232 (**Table M2** for further description of this antibody), and 4) an anti-GFP antibody recognizing the
233 C-terminus of Fn1-mEGFP protein. In our analyses, we focused on long fibrillar adhesions that
234 were over 1 μm in length, characteristic of mature assembled Fn1 fibrils (Lu et al., 2020).

235 Independent of the antibodies used, Fn1 fibrils appeared as arrays of periodically-
236 spaced nanodomains (**Figs. 5-6**). To ensure that the beaded appearance of fibrils was not due
237 to under-sampling, we tested 2 – 4 dilutions of each antibody, followed by SMLM imaging and
238 autocorrelation analysis, as in (Fruh et al., 2015). Our analyses showed that nanodomain
239 periodicity remained constant at all antibody dilutions tested (**Fig. 5, 6A"-E', summarized in**
240 **6F**). The periodicity of nanodomains detected with either R457, R184, or Abcam monoclonal
241 antibodies was similar to that measured with the anti-GFP antibody, suggesting that each of
242 these antibodies was used at the ELE comparable with that of GFP-labeling reagents. The
243 finding that nanodomain periodicity was independent of antibody specificity supports the
244 conclusion that the beaded appearance of Fn1 fibrils is not a result of a particular Fn1 protein
245 conformation, since staining using antibodies to three different regions of Fn1 in addition to
246 antibodies to GFP resulted in the same pattern. In all cases, nanodomain periodicity was
247 independent of the antibody concentrations, arguing against under-sampling (Fruh et al.,
248 2015).

249 Analysis using DBSCAN (Caetano et al., 2015) discovered clusters corresponding with
250 nanodomains, when the radius of the neighborhood (ε) was set to 14 nm, the average
251 apparent radius of an Fn1 nanodomain (**Table 2**, compare (**Figs. 7A and B**). Unbiased

252 DBSCAN clustering using the neighborhood radius that was automatically estimated by the
253 SMAP software discovered larger clusters of Fn1 nanodomains (**Fig. 7C**). This suggests that
254 Fn1 nanodomains are organized in a higher-order structure within long fibrils, consistent with
255 the observation of "beads" in lower-resolution diffraction-limited images of Fn1 (**Figs. 1, 2** and
256 **Sup. Figs. 3, 5, 6**).
257
258 **Fn1 nanodomains contain multiple full-length Fn1 molecules.**
259 It was previously-thought that Fn1 nanodomains detected by immunoelectron
260 microscopy or by immunofluorescence SMLM corresponded with particular regions in Fn1
261 protein sequence (Dzamba and Peters, 1991; Fruh et al., 2015), illustrated in **Sup. Fig. 8A-B**.
262 Surprisingly, staining using 297.1 polyclonal anti-Fn1 antibody raised against full-length
263 plasma Fn1 and recognizing multiple epitopes along Fn1 protein resulted in the same
264 periodicity of nanodomains as staining with antibodies to distinct regions of Fn1 protein (**Figs.**
265 **6E, 6F, Figs. 8A, 8D**). Since 297.1 polyclonal antibody recognizes multiple epitopes along
266 Fn1, including an epitope in the 70 kDA N-terminal assembly region of Fn1 (**Sup. Fig.4**), these
267 experiments suggested that each Fn1 nanodomains contained at least one entire Fn1 dimer.
268 To determine the number of Fn1 molecules per nanodomain, we used the methodology
269 developed by (Thevathasan et al., 2019), and identical labeling reagents and imaging
270 conditions for the detection of mEGFP in NUP96-mEGFP and Fn1-mEGFP cells (Thevathasan
271 et al., 2019). This analysis indicates that each Fn1 nanodomain contains 16.85 +/- 5.1 mEGFP
272 proteins on average (**Table 2).** Since Fn1 assembled in ECM fibrils is an obligate dimer of two
273 disulfide-bonded Fn1 molecules (Schwarzbauer, 1991), these findings show that Fn1
274 nanodomains contain 6 – 11 Fn1-mEGFP dimers, on average.
275 These results are not consistent with the model that thinnest Fn1 fibrils are made of
276 extended single Fn1 molecules that are periodically aligned in a regular, end-to-end fashion
277 with regions containing N-termini alternating with regions containing C-termini (Chen et al.,

278 1997; Dzamba and Peters, 1991; Fruh et al., 2015) and illustrated in **Sup. Fig. 8A-B**. Such
279 periodic alignment of Fn1 dimers necessitates that staining using antibodies recognizing
280 multiple epitopes along the length of Fn1 molecule would result in a uniform labeling of Fn1
281 fibrils, (**Sup. Fig. 8C**). However, this is not what we observed: staining with a polyclonal 297.1
282 antibody showed that Fn1 fibrils were composed of periodically-spaced nanodomains (**Fig. 8A-**
283 **A", 8D**). Autocorrelation analysis showed that the spacing was periodical at multiple
284 concentrations of 297.1 antibody (**Figs. 6E-E", 6F,** and **8D**). Importantly, the periodicity of
285 nanodomains detected using 297.1 antibody was statistically indistinguishable from
286 periodicities seen with any regions-specific antibody tested, including that of anti-GFP
287 antibodies (**Fig. 6F**). The latter suggested that 297.1 polylconal antibodies were used at an
288 ELE that was at least as high as that for GFP labeling reagents. Finally, the periodical
289 distribution of 297.1 epitopes (average periodicity 121±11) and the presence of multiple Fn1
290 dimers per nanodomain, does not fit with the model proposed by (Dzamba and Peters, 1991),
291 illustrated in **Sup. Fig. 8A**, and suggest a different model of Fn1 fibrillogenesis (e.g., **Fig. 8G**).
292 To further evaluate the hypothesis that Fn1 nanodomains contain full-lengths Fn1
293 dimers, we used combinations of antibodies and the imaging parameters resulting in the high
294 ELE (**Fig. 6F** and Methods). We first stained Fn1$^{mEGFP/mEGFP}$ MEFs using a combination of
295 R457 and anti-GFP antibodies, detecting the N- and C- termini of Fn1-mEGFP, respectively.
296 Consistent with the staining using 297.1 antibody, the periodicity of nanodomains detected with
297 a mixture of R457 and anti-GFP antibodies was 101±45 nm, which is statistically
298 indistinguishable from the periodicities when either of these antibodies were used alone (**Figs.**
299 **6F, 8B-B", 8E**).
300 Next, we stained Fn1$^{mEGFP/mEGFP}$ MEFs with a cocktail of five antibodies recognizing
301 epitopes distributed along the length of the Fn1 molecule: 1) the N-terminal 70 kDa assembly
302 domain of Fn1 (R457), 2) the sequence immediately following the 70 kDA domain (R184), 3)
303 an epitope in the middle of Fn1 (Abcam monoclonal), 4) multiple epitopes along the Fn1

304 protein (297.1), and 5) the anti-GFP antibody marking the C-terminus of Fn1-mEGFP (αGFP)
305 **(Fig. 8C-C", 8F**). Each antibody was used at a dilution resulting in a periodical staining (**Fig.**
306 **6F** and legend). The binding of all primary antibodies in the cocktail was detected by a cocktail
307 of Alexa 647-conjugated secondary antibodies. If Fn1 fibrils were indeed composed of
308 continuous, linear arrays of extended and periodically aligned Fn1 molecules, this cocktail of
309 antibodies recognizing epitopes from the N- to the C-termini of Fn1 would uniformly label Fn1
310 fibrils. Even in the scenario in which R457 epitopes did not extend to the N-terminal-most
311 sequence of Fn1, the staining using this mixture of five antibodies would not be expected to
312 produce periodical staining. However, we observed that the cocktail of 5 antibodies labeled
313 nanodomains with the average periodicity of 94±47 nm at the spatial resolution of 23 nm in thin
314 Fn1 fibrils (**Fig. 8C-8C", 8F**). This periodicity was statistically indistinguishable from the
315 periodicities of individual antibodies at all the dilutions tested (**Fig. 6F**).
316 Unbiased clustering using the Voronoi tessellation method (Andronov et al., 2016b)
317 implemented in SMAP showed that Fn1 fibrils stained with the 5-antibody cocktail can be
318 segmented into clusters (**Fig. 8C", 8C"-1**). This analysis shows that the nanodomain structure
319 of Fn1 fibrils can be discovered using an unbiased computational approach. The size of the
320 nanodomains detected with the 5-antibody cocktail was larger than when nanodomains were
321 detected by the use of any single antibody (e.g., compare **Fig. 8A"** with **Fig. 8C"**). This type of
322 behavior is expected in SMLM when molecules are clustered (Baumgart et al., 2016).
323 In agreement with the results described above, periodically-spaced nanodomains were
324 detected in Fn1 fibrils using two other cell lines, heterozygous $Fn1^{mEGFP/+}$ MEFs and wild-type
325 MEFs (**Sup. Fig. 9**). The presence of the periodical nanodomains in fibrils produced by wild-
326 type cells indicates that the periodical structure of Fn1 fibrils is not an artifact of GFP labeling.
327 Nanodomain spacing in Fn1 fibrils treated with 2% DOC, which removes cells and cellular
328 components, was similar to that of untreated fibrils (**Sup. Fig. 9,** columns **4** and **8,** and **Sup.**

329 **Fig. 9F**). Together, these data indicate that the nanodomain architecture of Fn1 fibrils is
330 independent of antibody(ies) used for staining, is seen in cells expressing wild-type Fn1 and in
331 the absence of cell contact, and that periodically-spaced nanodomains within Fn1 fibrils
332 contain multiple Fn1 dimers (e.g., model in **Fig. 8G**).

333 To further test the hypothesis that Fn1 nanodomains contain full-length Fn1 molecules,
334 we performed double-color dSTORM experiments, wherein the N-terminus of Fn1 was labeled
335 with the R457 primary antibody and anti-rabbit CF680-conjugated secondary immunoglobulins,
336 and the C-terminus of Fn1-mEGFP was labeled with the anti-GFP primary antibody and Alexa-
337 647-conjugated anti-chicken secondary antibodies. As a control, we stained $Fn1^{mEGFP/mEGFP}$
338 MEFs using two different anti-GFP antibodies, one made in rabbit (detected using CF680-
339 conjugated secondary antibodies) and the other, in chicken (detected with Alexa-647-
340 conjugated anti-chicken secondary antibodies). The majority of nanodomains detected using
341 the two anti-GFP antibodies contained overlapping CF680 and AF647 localizations, suggesting
342 a high ELE for both reagents (**Fig. 9A-C,C'**; Gray lines in **Fig. 9A', 9B'** mark overlapping
343 staining in nanodomains). Nanodomains in which the two labels did not overlap were marked
344 by purple lines (**Fig. 9A', 9B'**). To determine the extent of co-localization between the two
345 labels, we performed coordinate-based colocalization (CBC) analysis, a widely-accepted
346 method for detecting co-localization in SMLM data (Malkusch et al., 2012). The CBC
347 coefficient was calculated by counting the number of CF680 localizations within a radius *r* of
348 each of the AF647 localizations and normalizing by the number of localizations within the area
349 πR^2_{max} (Malkusch et al., 2012) (**Fig. 9D,F**). Conversely, we also determined the CBC coefficient
350 by counting the number of AF647 localizations within a radius *r* of each of the CF680
351 localizations and normalizing by the number of localizations within the area πR^2_{max} (**Fig. 9E,F**).
352 The CBC coefficients were calculated using algorithms implemented either by the Abbelight
353 software or by the publicly-available ThunderSTORM software (Ovesny et al., 2014). The

354 coefficient "+1" indicates a high probability of co-localization, while CBC ≤ 0 indicates low
355 probability of co-localization. CBC analysis using the Abbelight software and color-coding
356 according to the CBC coefficient, showed that the parameters chosen for these analyses,
357 r=30nm and R_{max}=300nm, reflect the overlap (e.g., yellow color in **Fig. 9D-E** and gray lines in
358 **Fig. 9A'-B'**) and the lack of overlap (purple color and arrows in **Fig. 9D-E** and purple lines and
359 arrows in **Fig. 9A'-B'**) seen in SMLM images. These figures also show that we can detect non-
360 overlapping signals in nanodomains located next to one another (**Fig. 9D-F**). CBC analyses
361 performed on twenty-two regions containing long (≥1μm) Fn1 fibrils from $Fn1^{mEGFP/mEGFP}$ MEFs
362 showed extensive overlap among localizations arising from rabbit and chicken anti-GFP
363 antibodies (**Fig. 9F**).
364 CBC analyses of twenty regions containing long fibrils from $Fn1^{mEGFP/mEGFP}$ MEFs
365 stained with R457 and anti-GFP antibodies showed extensive overlap between R457 and anti-
366 GFP localizations, detecting the N- and the C- termini of Fn1-mEGFP, respectively (**Fig. 9G-**
367 **L**). Using ThunderSTORM software, we varied the parameters of CBC analysis, e.g., setting
368 the radius r from 2 or 5 nm and R_{max} from 20 or 50nm, respectively. These analyses had the
369 same outcome as above, i.e., CBC coefficients were close to +1, indicating a high probability
370 of overlap among localizations resulting from R457 and anti-GFP antibody binding (**Sup. Fig.**
371 **10**). Together, these studies show that the N- and the C-termini of Fn1 are contained within
372 each Fn1 nanodomain and support the model wherein Fn1 nanodomains in Fn1 fibrils contain
373 multiple full-length Fn1 molecules (**Fig. 8G**).
374

375 **Nanoarchitecture of Fn1 fibrils formed by ectopically-added Fn1**

376 It is known that ectopic Fn1 added to cells becomes assembled into fibrils (McKeown-
377 Longo and Mosher, 1983). To determine whether fibrils incorporating ectopically-added Fn1
378 contain nanodomains, we first used live imaging to film the assembly of ectopic Fn1. In these

379 experiments, MEFs producing Fn1-mEGFP were cultured on the uncoated glass inside an
380 insert while a confluent monolayer of MEFs producing Fn1-tdTomato was grown in the space
381 surrounding the insert. Prior to imaging, the insert was lifted, and Fn1-mEGFP+ MEFs were
382 imaged at ~17 min intervals for 16 hours. These movies show that Fn1-tdTomato fibrils
383 become clearly visible on the surface of Fn1-mEGFP cells by about 3 hours of co-culture
384 without first accumulating inside cells, suggesting that ectopic Fn1 is assembled into fibrils at
385 the cell surface (**Movie 4**). To determine the nanoarchitecture of Fn1 fibrils formed by
386 ectopically-added Fn1, we cultured $Fn1^{mEGFP/mEGFP}$ MEFs in the presence of 10 μg of Fn1-
387 tdTomato for 24 hours. Cells were fixed and stained without permeabilization using rabbit anti-
388 Cherry primary antibodies and anti-rabbit Alexa647-conjugated secondary antibodies. ECM in
389 regions between cells was imaged using TIRF to detect Fn1-mEGFP and Fn1-tdTomato
390 fluorescence, and dSTORM to detect Fn1-tdTomato due to the Alexa 647 label. Fn1-tdTomato
391 extensively co-assembled with Fn1-mEGFP (**Sup. Fig. 11A-B**), and high-resolution SMLM
392 reconstructions of thin and thick fibrils contained nanodomain arrays composed of Fn1-
393 tdTomato proteins (**Sup. Fig. 11C-E, 11F)**. Together, these experiments demonstrate that 1)
394 Fn1 fibrils deposited into the intercellular ECM space are composed of nanodomain arrays and
395 2) ectopic Fn1 assembles into fibrils comprised of nanodomain arrays.
396

397 **Fibrillogenesis inhibitor FUD disrupts the organization of Fn1 nanodomains into**
398 **periodical arrays**

399 To understand the relationship between the nanodomain architecture of Fn1 fibrils and
400 the process of fibrillogenesis, we adopted a live imaging approach using $Fn1^{mEGFP/+}$ MEFs and
401 inhibitors of fibrillogenesis. One such inhibitor is a 49-amino acid peptide derived from
402 *Streptococcus pyogenes* adhesin F1, termed the functional upstream domain (FUD), a highly
403 potent inhibitor of Fn1 fibrillogenesis (Tomasini-Johansson et al., 2001). Fn1 fibrillogenesis

404 critically depends on the interactions mediated by the N-terminal 70 kDa assembly domain of
405 Fn1 (**Fig. 4A**), and FUD is one of the inhibitors that interferes with these interactions (Filla et
406 al., 2017; Morla et al., 1994; Schwarzbauer, 1991; Sechler et al., 2001; Sechler et al., 1996;
407 Tomasini-Johansson et al., 2001).

408 To further investigate the mechanism of Fn1 fibrillogenesis and the role of the N-
409 terminal domain of Fn1 in this process, Fn1$^{mEGFP/+}$ MEFs were plated on uncoated glass for 4
410 hours, and then imaged for 15 – 18 hours either in the imaging medium alone, or in the
411 medium containing 225 nM FUD. We also imaged cells incubated with 274 nM 11-IIIC peptide,
412 a 68 amino-acid control peptide that does not interfere with Fn1 fibrillogenesis (Morla et al.,
413 1994; Sottile and Chandler, 2005). Untreated cells or cells treated with the control peptide
414 developed and accumulated long Fn1 fibrils (**Movie 5**). In contrast, treatment with FUD led to
415 a) the dismantling of the pre-existing Fn1 fibrils and b) inhibiting the formation of new Fn1
416 fibrils (**Movie 6)**. Instead of fibrils, cells cultured in the presence of FUD mainly contained
417 centripetally-moving Fn1-mEGFP fluorescent "beads" that only rarely assembled into fibrils
418 (**Movie 6**). These experiments suggested that FUD inhibits fibrillogenesis by interfering with
419 the process by which Fn1 "beads" become arranged or connected into linear arrays. To test
420 this hypothesis, Fn1$^{mEGFP/+}$ MEFs were plated for 16 hours in the continuous presence of either
421 225 nM FUD or 274 nM III-11C control peptides or were left untreated. Cells were then washed
422 with PBS, fixed, and stained without permeabilization using monoclonal anti-Fn1 antibodies
423 and Alexa Fluor 647-conjugated secondary antibodies, and imaged at the critical angle of
424 incidence by STORM (Jimenez et al., 2020). This approach maximizes the detection of cell-
425 surface Fn1 due to: a) the absence of a detergent during fixation, staining and washing and b)
426 imaging at the critical angle of incidence to detect fluorescence in close proximity to the
427 plasma membrane. These experiments demonstrated that the organization of Fn1
428 nanodomains into linear arrays was lost upon incubation with FUD (compare **Fig. 10A, B, A1,**
429 **B1** with **Fig. 10C, C1**). Non-fibrillar (NF) Fn1 nanodomains in cells treated with FUD had a

430 similar number of Fn1 localizations per nanodomain, and were of similar sizes compared with
431 fibrillar or non-fibrillar Fn1 nanodomains in untreated cells, or cells incubated with the control
432 peptide (**Fig. 10A2, 10B2, 10C2**, **10D**). Taken together, these data indicate that FUD does not
433 interfere with the formation of Fn1 nanodomains but inhibits the organization of Fn1
434 nanodomains into linear arrays. Since Fn1 proteins lacking the N-terminal assembly domain do
435 not form fibrils (Schwarzbauer, 1991), our experiments suggest that interactions mediated by
436 the N-terminal assembly domain of Fn1 with a yet unidentified factor(s), are critical for the
437 organization of Fn1 nanodomains into fibrillar arrays (**Fig. 10E** and *vide infra*).
438

439 **Discussion**

440 In this manuscript, we describe data supporting a novel mechanism underlying the process of
441 Fn1 fibrillogenesis. In this model, 6-11 Fn1 dimers assemble into nanodomains containing
442 integrin $\alpha5\beta1$ at the cell periphery, move rearward with actin flow, and become organized into
443 linear arrays of periodically-spaced nanodomains. Joining of the additional Fn1 nanodomains
444 to these arrays leads to the generation of longer and longer fibrils as nanodomain assemblies
445 move toward the cell center. We show that these periodical nanodomain assemblies are bona
446 fide Fn1 fibrils.

447 The N-terminus of Fn1 is essential for Fn1 fibrillogenesis (Schwarzbauer, 1991). FUD
448 binds tightly to the N-terminal domain of Fn1 (K_D<2.6 nM), with a fast k_{on} and a slow k_{off}, and
449 acts as a competitive inhibitor of Fn1-Fn1 interactions (Ma et al., 2015; Maurer et al., 2010;
450 Tomasini-Johansson et al., 2001). Although in the absence of FUD, individual fibrils in an
451 established matrix are stable and can be tracked for over 16 hours (S.A., unpublished
452 observations), when FUD is added to cells, it localizes with Fn1 fibrils and dismantles the
453 mature Fn1 ECM (Filla et al., 2017; Tomasini-Johansson et al., 2001). These findings suggest
454 that the fibrillar $Fn1^+$ ECM is maintained through dynamic interactions mediated by the 70 kDa

455 Fn1 N-terminal domain. Our live imaging experiments demonstrated that in addition to
456 dismantling pre-existing fibrils, FUD effectively blocks their de-novo formation. SMLM showed
457 that FUD does not affect the formation of Fn1 nanodomains, instead, it blocks the organization
458 of Fn1 nanodomains into linear arrays. Together, these data suggest that FUD blocks the
459 dynamic interactions between the N-terminal Fn1 assembly domain and factor(s) linking Fn1
460 nanodomains into fibrils.

461 Previously, the periodical distribution of domain-specific antibody epitopes in EM and
462 SMLM images of Fn1 fibrils was explained by a model stipulating that Fn1 fibrils are made of
463 aligned and extended Fn1 molecules (Dzamba and Peters, 1991) (**Sup. Fig. 8A-B**). In EM
464 micrographs of Fn1 molecules sprayed onto mica surface, one can see extended Fn1 dimers
465 that are on average 120-140 nm in length (Engel et al., 1981; Erickson et al., 1981). Therefore,
466 it was hypothesized that spacing of ~84 nm seen in EM with domain-specific antibodies
467 (Dzamba and Peters, 1991) or spacing of ~100 nm in SMLM images (Fruh et al., 2015) was
468 due to the overlap between the extended Fn1 molecules at their N-termini (Dzamba and
469 Peters, 1991), e.g., (**Sup. Fig. 8B,** overlap marked by a bubble). The findings that the N-
470 terminal 70 kDa domain is required for Fn1 fibrillogenesis, that this domain can mediate
471 intermolecular Fn1-Fn1 interactions, and that inhibitors of Fn1 fibrillogenesis bind to this
472 domain were interpreted in favor of this model. However, these biochemical data are also
473 consistent with a very different model of Fn1 fibrillogenesis (**Sup. Fig. 8**), one that was
474 proposed by (Tomasini-Johansson et al., 2006) and discussed below.

475 A canonical model poses that Fn1 fibrillogenesis entails intermolecular Fn1-Fn1
476 interactions mediated by the 70 kDa N-terminal domain of Fn1 (Hocking et al., 1994; Zhong et
477 al., 1998), summarized in (Singh et al., 2010). These interactions were hypothesized to be
478 important for linking extended Fn1 dimers into fibrils (e.g., **Sup. Fig. 8A**). It was stipulated that
479 FUD blocks Fn1 fibrillogenesis because of its ability to compete with Fn1-Fn1 intermolecular
480 interactions and disassemble fibrils by inhibiting intermolecular interactions between Fn1

481 dimers (**Sup. Fig. 8D**). However, these biochemical and cell biological experiments are also
482 consistent with a different model, wherein Fn1 fibrillogenesis is mediated by the binding of the
483 70 kDa N-terminal domain to large apparent molecular mass cell-surface complexes (LAMMs)
484 (Tomasini-Johansson et al., 2006; Zhang and Mosher, 1996) (**Sup. Fig. 8E**), and that FUD can
485 disrupt fibrillogenesis by disrupting the interactions between the 70 kDa Fn1 assembly domain
486 and LAMMs (**Sup. Fig. 8E**). Biochemical evidence supporting this model is multifold: 1)
487 isolated 70 kDa N-terminal domain can bind to Fn1-null cells in the absence of Fn1, forming
488 short linear arrays; this binding is time- and dose-dependent, and is detectable with as little as
489 5 nM of 70 kDa N-terminal segment of Fn1 (Tomasini-Johansson et al., 2006); 2) Incubation of
490 the 70 kDa domain of Fn1 with cells precipitates LAMMs in pull-down assays (Zhang and
491 Mosher, 1996); 3) LAMMs contain trypsin-sensitive protein(s) (Zhang and Mosher, 1996); and
492 4) FUD inhibits the binding of 70 kDa N-terminal fragment to Fn1-null cells (Tomasini-
493 Johansson et al., 2006). These findings suggest that Fn1 nanodomains in fibrils can be held
494 together by the interactions between the 70 kDa N-terminal assembly domain of Fn1 and
495 LAMMs (**Sup. Fig. 8F1**). However, at this time, we cannot rule out a possibility that Fn1
496 nanodomains are held by an extended Fn1 molecule via N-N-terminal interactions (**Sup. Fig.**
497 **8F2**), or that a combination of the latter two models may be true.

498 Our model in which Fn1 fibrils are composed of periodically-spaced nanodomains
499 containing multiple Fn1 dimers is also supported by electron microscopy and atomic force
500 microscopy studies done in the past: 1) periodical staining of Fn1 fibrils was observed in EM
501 with polyclonal antibodies raised to entire human plasma Fn1 (Furcht et al., 1980a); 2) grapes-
502 on-a-vine appearance of immuno-gold complexes detecting plasma Fn1 in fibrils in electron
503 micrographs (Peters et al., 1990); 3) bulbous appearance of Fn1 fibrils in cryo-scanning
504 transmission electron tomography images (Lansky et al., 2019); and 4) beaded appearance of
505 Fn1 fibrils detected by atomic force microscopy (Gudzenko and Franz, 2015). The latter two

506 methods did not rely on antibody staining to detect Fn1 nanodomains, supporting the notion
507 that the beaded architecture of Fn1 fibrils is not an artifact of antibody labeling.
508 Together with our data, these experiments suggest a new model of Fn1 fibrillogenesis
509 (**Fig. 10E**). In this model, Fn1 nanodomains containing multiple Fn1 dimers form at cell
510 periphery. These nanodomains may be similar to focal complexes or adhesion-related particles
511 seen by cryo-electron tomography by (Patla et al., 2010). The centripetal translocation of Fn1
512 nanodomains is coordinated with their organization into linear arrays, giving rise to focal
513 adhesions composed of ~3-5 Fn1 nanodomains and long Fn1 fibrillar adhesions composed of
514 dozens of nanodomains. Fn1 fibrils generated in this process are then incorporated into Fn1
515 ECM (Mautner and Hynes, 1977; Pankov et al., 2019; Sivakumar et al., 2006). Two pieces of
516 evidence suggest that Fn1 nanodomains in fibrils are linked: 1) the preservation of the linear
517 organization and the nanoarchitecture of Fn1 fibrils after the treatment of cells with DOC which
518 dissolves cell membranes, and 2) the presence of fibrous material between immunogold
519 densities in electron micrographs (Chen et al., 1997; Dzamba and Peters, 1991; Furcht et al.,
520 1980a; Furcht et al., 1980b; Furcht et al., 1980c; Lansky et al., 2019; Peters et al., 1990). The
521 sparsity of Fn1 localizations between Fn1 nanodomains in fibrils suggests that molecules other
522 than or in addition to Fn1 participate in the potential linking of Fn1 nanodomains into periodical
523 nanodomain arrays.
524 The beaded architecture of Fn1 ECM has important implications for the mechanisms of
525 ECM formation, remodeling, and signal transduction. The tensile strength of knotted strings is
526 significantly lower than that of strings with uniformly-aligned fibers (Arai et al., 1999; Saitta et
527 al., 1999), thus the beaded architecture of Fn1 fibrils may facilitate their rupture under strain
528 (Ohashi et al., 1999). The non-uniform, nanodomain architecture of Fn1 may facilitate the
529 accessibility of Fn1 fibrils to matrix metalloproteases. In this model, degradation of Fn1 fibrils
530 by metalloproteases may be accomplished by the cleavage of LAMMs between Fn1
531 nanodomains facilitating dynamic ECM remodeling. Finally, Fn1 is known to bind growth

532 factors (Martino and Hubbell, 2010; Saunders and Schwarzbauer, 2019; Wijelath et al., 2002),
533 and cell adhesion to ECM is known to orchestrate growth factor signaling (Hynes, 2009). Thus,
534 Fn1 nanodomains could serve as platforms for the binding and presentation of concentrated
535 packets of growth factors to cells, the organization of Fn1 nanodomains into closely-spaced
536 arrays could further facilitate clustering and signaling by growth factor receptors.
537

538 **Acknowledgments**

539 We thank Richard Hynes and Nathan Astrof for insightful discussions and careful reading of
540 the manuscript, Sydney Astrof for encouragement and help with data entry, Patrick Murphy for
541 endothelial cells, Richard Hynes for the gift of 297.1 antibody, Tung Chan for help with setting
542 up Western Blotting using ProteinSimple, and Jonas Ries for advice that helped us improve
543 SMLM resolution of our imaging, and for his help with adopting the SMAP software. Epitope
544 mapping of 297.1 antibody was performed by PEPperPRINT GmbH, Heidelberg, Germany.
545

546 **Sources of Funding** This work was supported by the funding from the National Heart, Lung,
547 and Blood Institute of the NIH R01 HL103920, R01 HL134935, R01 HL158049, American
548 Heart Association Transformative Project Award 20TPA35490074 to SA, and by the NIH Office
549 of the Director R21 OD025323-01 to SA, by the pre-doctoral fellowship F31HL151046 to BEA,
550 by the National Institute of General Medicine R35GM122505 to AK, by the National Institute of
551 Arthritis and Musculoskeletal and Skin Diseases R01 AR073236 to JES, by the Faculty Seed
552 Grant from the Center for Engineering MechanoBiology (CEMB), an NSF Science and
553 Technology Center, under grant agreement CMMI: 15-48571. Any opinions, findings, and
554 conclusions or recommendations expressed in this material are those of the authors and do
555 not necessarily reflect the views of the National Science Foundation.

556

557 **Materials and Methods**

558 **Generation Fn1-fluorescent protein targeting constructs** Sequences of monomeric (m)
559 green fluorescent protein (GFP), mNeonGreen, mScarlet-I, and tdTomato were obtained from
560 FPbase (https://www.fpbase.org). The sequence encoding one of the above fluorescent
561 proteins (FPs) was knocked into the Fn1 locus following the last coding exon of mouse Fn1,
562 and separated from the last coding amino acid by a flexible, proline-rich linker, PPPELLGGP
563 (Snitkovsky and Young, 1998). Targeting was achieved by CRISPR/Cas9 (Ran et al., 2013).
564 The sequence of the guide RNA was chosen and off-target sites were identified using
565 GuideScan and Off-Spotter software (Perez et al., 2017; Pliatsika and Rigoutsos, 2015). The
566 guide RNA (gRNA) sequence 5'-AGC GGC ATG AAG CAC TCA AT-3' targeting the last
567 coding exon of *Fn1* was subcloned downstream the U6 promoter into the PX459 vector
568 (Addgene, cat # 62988) encoding the Cas9-2A-Puromycin cassette (Ran et al., 2013). The
569 homology-directed repair (HDR) template was constructed using pBS-KS vector (Sup. Fig. 1a).
570 The sequence of the last coding exon of *Fn1* 5'-
571 AACGTAAATTGCCCCATTGAGTGCTTCATGCCGCTAGATGTGCAAGCTGACAGAGACGAT
572 TCTCGAGAG-3' was modified to 5'-
573 AACGTAAATTGCCCCATcGAaTGCTTCATGCCGCTAGATGTGCAAGCTGACAGAGACGATT
574 CTCGAGAG-3' in the HDR template by introducing silent mutations (underlined) to prevent
575 targeting of the template by the gRNA. Homology arm 1 contained 677 bp encoding exon #45,
576 intron, and a portion of the last exon (#46), of the transcript *ENSMUST00000055226.12*.
577 Homology arm 2 encoded 1739 bp immediately downstream of the *Fn1* termination codon and
578 included the unmodified 3'UTR of Fn1. Knockin Fn1$^{mEGFP/+}$ mice were generated by
579 Biocytogen using the same HDR construct and a longer gRNA, 5'-TAG CGG CAT GAA GCA
580 CTC AAT GG-3',
581 targeting the same sequence in the last coding exon (differences between the two gRNAs are
582 underlined). Targeting was confirmed by sequencing and Southern Blotting

583 (Sub. Fig. 1b). 500 bp around each of the top ten predicted off-target sites were sequenced
584 and no mutations were found in the founder mice. Mice containing correctly-targeted *Fn1* locus
585 were used to establish living colonies of $Fn1^{mEGFP/mEGFP}$ animals. Wild-type, $Fn1^{mEGFP/+}$, and
586 $Fn1^{mEGFP/mEGFP}$ mice were genotyped using the following primers Fn1-WT-Fwd 5'-
587 TCCCCGAAACACACACACTTTTGGT-3', Fn1-WT-Rev 5'
588 GTCACCCTGTTCTGCTTCAGGGTTT-3', and Fn1GFP-Rev 5'-
589 GACCCGCGCCGAGGTGAAG-3'. Wild type band is Fn1-WT-Fwd and Fn1-WT-Rev give rise
590 to 372 bp for the wild-type allele; Fn1-WT-Fwd and Fn1GFP-Rev primer located in the GFP
591 sequence give rise to 512 bp if the targeted allele is present. Mice were housed in an
592 AAALAC-approved barrier facility. All experimental procedures were approved by the
593 Institutional Animal Care and Use Committee of Rutgers University and conducted in
594 accordance with the Federal guidelines for the humane care of animals.
595
596
597 **Cell Culture**
598 **Table M1. Media**

	Cells	Composition of Medium
Complete medium	MEFs	High-glucose Dulbecco's Modified Eagle Medium (DMEM, Corning, cat # 10-013-CV) supplemented with 10% v/v fetal bovine serum (Gemini Biosciences, cat # 100-106), 1% v/v penicillin/streptomycin solution (GE Healthcare, cat #SV30010), 1% v/v L-glutamine (Gibco, cat # 35050-061).

Imaging medium	MEFs	FluoroBrite DMEM (Thermo Fisher Scientific, catalog # A1896701) supplemented with 2% v/v fetal bovine serum (Gemini Biosciences 100-106), 1% v/v penicillin/streptomycin solution (GE Healthcare, SV30010), 1% v/v L-glutamine (Gibco 35050-061), pH8.14.
McCoy's 5a	Nup96-mEGFP U2OS cells	McCoy's 5a medium containing 1xGlutaMax (ThermoFisher, cat #35050061), 10% v/v fetal bovine serum (Gemini Biosciences, cat # 100-106), and 1x penicillin/streptomycin (GE Healthcare, cat #SV30010).

599

600 **Cells** Wild-type mouse embryonic fibroblasts (MEFs) were isolated from embryonic day (E)
601 13.5 embryos derived from the C57BL/6J strain (Jackson Labs, stock # 664) according to
602 established protocols (Behringer et al., 2014) and cultured in complete medium. For
603 propagation, MEFs were plated in flasks pre-coated with 0.1% gelatin solution and grown in
604 complete medium at 37°C, 5% CO_2.

605 $Fn1^{flox/+}$;$Rosa^{mTmG/+}$ MEFs were isolated from E13.5 embryos, as above, and express
606 membrane-bound tdTomato and wild-type Fn1 in the absence of Cre recombinase (Muzumdar
607 et al., 2007). Fn1-null MEFs were generated by treating $Fn1^{flox/-}$;$Rosa^{mTmG/+}$ cells with Ad-Cre-
608 IRED-GFP virus according to the manufacturer's recommendations (Vector Biolabs, #1710). In
609 this experiment, Cre-recombinase is expressed transiently and mediates site-specific
610 recombination between a pair of loxP sites flanking the 1st exon of Fn1 (Sakai et al., 2001) and
611 another pair of loxP sites flanking the STOP cassette in the mTmG reporter (Muzumdar et al.,

612 2007). Three days following infection with Ad-Cre-IRED-GFP, GFP+ cells were sorted resulting
613 in a pure population of Fn1-null MEFs (confirmed by Western Blotting, data not shown, and
614 immunofluorescence, **Sup. Fig. 12**). Fn-null MEFs were culture on gelatin-coated dishes in
615 complete medium.

616 Fn1-FP cells (except Fn1-mEGFP cells) were generated by CRISPR/Cas9 mutagenesis
617 of wild-type MEFs. CRISPR/Cas9 targeting was performed by transfecting wild-type MEFs
618 using the PX459 plasmid encoding Fn1 gRNA and the HDR template using lipofectamine
619 3000, as described (Ran et al., 2013). MEFs expressing Fn1-mEGFP proteins used for live
620 imaging and STORM were generated from homozygous E13.5 $Fn1^{mEGFP/mEGFP}$ or, when noted
621 from $Fn1^{mEGFP/+}$ embryos. $Fn1^{mEGFP/mEGFP}$ MEFs were used to quantify Fn1 molecule number in
622 nanodomains, measure nanodomain spacing, and nanodomain diameter, as well as in
623 experiments to label both the N- and the C-termini of Fn1. For live imaging, $Fn1^{mEGFP/+}$ were
624 used. Fibronectins from $Fn1^{mEGFP/mEGFP}$ and $Fn1^{mEGFP/+}$ cells behave equivalently in Fn1 matrix
625 assembly assays (data not shown).

626 Nup96-mEGFP cells ((Thevathasan et al., 2019), clone #195, Cell Line Services, CLS,
627 clsgmbh.de, catalogue no. 300174)) were cultured according to the vendor's specifications in
628 McCoy's 5a medium containing 1xGlutaMax (ThermoFisher, cat #35050061), 10% v/v fetal
629 bovine serum (Gemini Biosciences, cat # 100-106), and 1x penicillin/streptomycin (GE
630 Healthcare, cat #SV30010).

631

632 **Reagents and buffers**

633 FUD and III-11C peptides were generated as described (Sottile and Chandler, 2005; Tomasini-
634 Johansson et al., 2001) and stored in PBS at -80° C. 4% DOC solution was prepared by
635 dissolving 0.4 g deoxycholate salt (Sigma, catalog # D6750) in 10 ml of imaging medium; the
636 solution was then vortexed and filter sterilized. The pH of the final solution was 8.01. 16%
637 paraformaldehyde (PFA) (Electron microscopy Sciences; catalog # 50-980-487) was diluted in

638 1x PBS to prepare 4% PFA. The 4% PFA solution was aliquoted into 1 ml microfuge tubes,
639 stored at -80° C, and thawed at 37° C immediately before use.
640
641 1X phosphate buffered saline pH 7.5 (PBS) was prepared from 10X PBS (VWR, catalog #
642 76180-740). PBST was prepared using Triton X-100 (Sigma-Aldrich, catalog # T-8787) and
643 contained 0.1% Triton for all stainings except those involving Nup96-mGEFP cells, as detailed
644 below. Blocking buffer was prepared by adding 10% Donkey serum (Sigma-Aldrich, catalog #
645 D9663) to 1X PBST; 5 mg/ml stock of DAPI (Fisher Scientific, cat #D3571) was prepared in
646 water and used at 1:300 dilution. Stain Buffer (cat # 554656 BD Pharmingen) was used for
647 antibody dilutions and washing of cells that were stained without permeabilization.
648 Hoechst 33342 Trihydrochloride (Thermo Fisher, catalog # H1399, 10mg/ml) was used for
649 labelling live MEFs at 1:300 dilution. In live MEFs, F-actin was labelled using SiR actin (cat#
650 CY-SC001 used at 1 μM final concentration). mCardinal-Lifeact-7 was a gift from Michael
651 Davidson (Addgene plasmid # 54663 ; http://n2t.net/addgene:54663 ; RRID:Addgene_54663).
652 Vectashield antifade mounting medium (Vectorlabs, catalog # H-1000) was used for cover
653 slipping.

654 For STORM imaging, we used 25 mm high precision glass cover slips #1.5H (Marienfeld ref#
655 0117650, obtained from Azer Scientific, PA, USA, cat # ES0117650) without coating. Prior to
656 their use, glass cover slips were cleaned using concentrated nitric acid, washed in water, air
657 dried, and autoclaved, as described in (Kaech and Banker, 2006). Clean coverslips were
658 stored in sealed 6-well plates for no longer than a week prior to their use.

659 GLOX/BME STORM buffer contained 50 mM Tris-HCl (Fisher Scientific, catalog # T-395-1),
660 pH 8.0, 10 mM NaCl (Sigma- Aldrich, catalog # S-7653), 10% glucose (Sigma- Aldrich, catalog
661 # G8270), 0.5 mg/ml glucose oxidase (Sigma- Aldrich, catalog # G2133), 40 μg/ml catalase

662 (Sigma- Aldrich, catalog # C40), and 143 mM β-mercaptoethanol (βME, Sigma-Aldrich, cat#
663 444203) (Thevathasan et al., 2019). Stocks of enzyme solutions were prepared and stored at -
664 20ºC as described in (Jimenez et al., 2020). GLOX/BME buffer was used for STORM imaging
665 of cells plated on coverslips.
666
667 GLOX/MEA STORM buffer was used for STORM imaging of cells plated in Ibidi glass bottom
668 8-well chambers (catalog # 80827). This buffer was prepared as above, but instead of βME, it
669 contained 50 mM mercaptoethylamine (MEA, Sigma-Aldrich, catalog # 30070) (Jimenez et al.,
670 2020). For double-color STORM imaging, we used the SMART Kit buffer (Abbelight).
671
672 **Antibodies**
673 All primary antibodies were checked for specificity on cells that were genetically-null for the
674 antigen (e.g., **Sup. Fig. 12**) and tissues: Fn1-null tissue sections obtained from Fn1-null
675 embryos were used to assay the specificity of each of the anti-Fn1 antibodies; Tissues isolated
676 from GFP-null, Itga5-null, and mCherry-null embryos were used to authenticate the specificity
677 of anti-GFP, anti-Itga5, and anti-mCherry antibodies. For each of the antibodies, staining of
678 control tissues resulted in no more fluorescent signal than the background fluorescence
679 produced by the use of secondary antibodies only. Rabbit polyclonal antibody R457 was raised
680 against the 70 kDa N-terminal domain of Fn1 (Aguirre et al., 1994; Sechler et al., 2001) and
681 rabbit polyclonal R184 was raised against the first six type III repeats of Fn1 (Raitman et al.,
682 2018).
683
684 **Table M2. Antibodies**

Primary Antibodies (1º Ab)	**Specificity**	**Source/ reference**

Abcam recombinant rabbit monoclonal	Epitope recognized by this antibody is located within 301 aa between amino acids 1350- 1651 of mouse Fn1, transcript variant 2, mRNA, RefSeq NM_001276408	Abcam, cat # 199056
297.1 rabbit polyclonal	Raised to rat plasma Fn1. Recognizes multiple epitopes, see **Sup. Fig. 4**	Richard Hynes lab (Rickelt and Hynes, 2018)
R457 rabbit polyclonal	70 kDa N-terminal domain	Jean Schwarzbauer's lab (Aguirre et al., 1994; Sechler et al., 2001)
R184 rabbit polyclonal	First six type III repeats of Fn1	Jean Schwarzbauer's lab (Raitman et al., 2018)
3E2 mouse monoclonal	EIIIA	Sigma, cat #SAB4200784-100UL
GFP, chicken polyclonal	GFP	Aves, cat# GFP-1010;
GFP, rabbit polyclonal	GFP	MBL International; cat #598
Itgα5, rat monoclonal	Integrin alpha 5	BD biosciences, cat # 553319
mCherry, rabbit polyclonal	Cherry; tdTomato is composed of two mCherry	Abcam, cat # ab167453

	molecules in tandem (Shaner et al., 2005)	

685

Secondary Antibodies (2° Abs)	Source, catalog #, concentration	Dilution
AffiniPure F(ab')$_2$ Fragment Donkey Anti-Rabbit IgG (H+L)	Jackson Immunoresearch, cat # 711-606-152, 1.5 mg/ml	1:300
Donkey anti-Mouse IgG (H+L) Highly Cross-Adsorbed Secondary Antibody, Alexa Fluor 555	ThermoFisher Scientific, A-31570, 2 mg/ml	1:300
Cy™3 AffiniPure F(ab')$_2$ Fragment Donkey Anti-Rat IgG (H+L)	Jackson Immunoresearch, 712-166-150, 1.5mg/ml	1:300
Alexa Fluor® 488 AffiniPure F(ab')$_2$ Fragment Donkey Anti-Chicken IgY (IgG) (H+L)	Jackson Immunoresearch, 703-546-155, 1.5mg/ml	1:300
Alexa Fluor® 647 AffiniPure F(ab')$_2$ Fragment Donkey Anti-Chicken IgY (IgG) (H+L)	Jackson Immunoresearch, 703-606-155, 1.5mg/ml	1:300

CF680 Donkey anti-rabbit, highly cross-adsorbed	Biotium, cat # 20418-50ul), 2mg/ml	1:200

686

687

688 **Epitope mapping of rabbit 297.1 polyclonal antibody.** Epitopes recognized by the
689 polyclonal 297.1 antibody were mapped by generating custom overlapping peptide arrays
690 (PEPperPRINT GmbH, Heidelberg). Fn1 protein sequence including alternatively-spliced
691 exons was encoded by 15-amino acid peptides with a peptide-peptide overlap of 13 amino
692 acids. The resulting Fn1 peptide microarrays contained 1,239 different peptides printed in
693 duplicate (2,478 peptide spots), and were framed by additional HA-tag (YPYDVPDYAG, 106
694 spots) control peptides. HA-tag peptide was used to monitor array quality and served as a
695 positive control for clean antibody binding detected with anti-HA-tag antibody (mouse
696 monoclonal anti-HA DyLight800 used at 0.5 µg/ml concentration). Prior to staining, arrays were
697 incubated with blocking buffer (Rockland, cat # MB-070) for 30 min at RT. To measure
698 background antibody binding, arrays were first incubated with secondary goat anti-rabbit IgG
699 (Fc) DyLight680 at 0.2 µg/ml concentration diluted in PBS, pH 7.4, containing 0.05% Tween 20
700 and 10% blocking buffer, and imaged. To determine specific 297.1 antibody binding, arrays
701 were incubated for 16 hours with shaking at 4°C with two dilutions of 297.1 antibody (1:300
702 and 1:1000). Antibody dilutions were made in PBS, pH 7.4 containing 0.05% Tween 20 and
703 10% blocking buffer (Rockland, cat # MB-070). Arrays were then washed with PBS, pH 7.4
704 containing 0.05% Tween 20 and incubated with goat anti-rabbit IgG (Fc) DyLight680 (0.2
705 µg/ml) for 45 min at RT. Arrays were then washed and imaged using LI-COR Odyssey Imaging
706 System; scanning offset 0.65 mm, resolution 21 µm, scanning intensities of 7/7 (red = 700
707 nm/green = 800 nm). Quantification of spot intensities and peptide annotation were done with
708 PepSlide® Analyzer.

709

710 **Embryo Staining** E9.5 embryos were isolated either from matings of wild-type C57BL6/J mice
711 or from mating $Fn1^{mEGFP/mEGFP}$ mice with wild-type mice to obtain $Fn1^{mEGFP/+}$ embryos.
712 Embryos were fixed using cold 4% PFA overnight at 4ºC, washed 3 x 5 min in 1xPBS, and
713 blocked overnight at 4ºC in blocking buffer containing PBS, 0.1% Triton-X, and 10% donkey
714 serum. Embryos were stained either with Abcam monoclonal anti-Fn1 antibodies at 1:300
715 dilution in blocking buffer or with both Abcam monoclonal anti-Fn1 antibodies and anti-GFP
716 antibodies at 1:300 dilution. The staining procedure was executed exactly as described in
717 (Ramirez and Astrof, 2020).

718

719 **Analysis of Fn1 matrix assembly** Matrix Assembly was performed according to the
720 established protocols (Wierzbicka-Patynowski et al., 2004). MEFs were plated in 6-well dishes
721 (9 cm^2 growth area) at a density of 2×10^5 cells per well for 48 h, in complete medium and
722 incubated under sterile conditions at 37°C, 5% CO2. Cells were washed twice with ice cold
723 PBS (supplemented with Mg^{2+} and Ca^{2+}), scraped with a cell scraper and lysed with either 500
724 μl RIPA lysis buffer pH 8.0 (50 mM Tris-Cl, 150 mM NaCl, 2 mM EDTA, 1% v/v NP-40, 0.5%
725 w/v sodium deoxycholate, 0.1% w/v SDS, 1X protease inhibitor cocktail (Cell Signaling
726 Technology, cat # 5871), or DOC lysis buffer, pH 8.8 (20 mM Tris-Cl, 2 mM EDTA, 2% w/v
727 sodium deoxycholate, 1X protease inhibitor cocktail (Cell Signaling Technology, 5871).
728 Extracts were carefully transferred to Eppendorf tubes containing 1 μl (250 units) Benzonase®
729 Nuclease (Sigma-Aldrich, E1014), mixed by inverting a few times and incubated at 37 ºC for
730 15 mins. The samples were then centrifuged at 16,000 × g for 15 min at 4 °C. For cells lysed
731 with DOC lysis buffer, the supernatant containing DOC-soluble material was carefully
732 removed, and the pellet containing the DOC-insoluble material was resuspended in 100 μl
733 SDS solubilization buffer, pH8.8 (20 mM Tris-Cl, 2 mM EDTA, 1% w/v SDS, 1X protease

734 inhibitor cocktail (Cell Signaling Technology, 5871). The DOC-insoluble pellet was thoroughly
735 dissolved by heating the sample to 95 ^{o}C and vortexing. All samples were aliquoted and stored
736 at -80 ^{o}C until further use. Prior to quantification of Fn1 in the samples, the total protein
737 concentration of the RIPA and DOC lysates was determined using the BCA protein assay
738 (Pierce™ BCA Protein Assay Kit, 23225). Fn1 and Fn1-FP fusion proteins were resolved using
739 66-440 kDa Wes separation module (ProteinSimple, SM-W007). Primary antibodies were used
740 at the following dilutions: anti-total Fn1 – 1:1000 (Abcam, ab199056), anti-GFP – 1:1000
741 (Roche, 11814460001), anti-mCherry – 1:1000 (Abcam, 167453). Primary antibodies were
742 detected using horseradish peroxidase-conjugated secondary antibodies (anti-Rabbit
743 Detection Module ProteinSimple, DM-001), and chemiluminescence was quantified using the
744 Compass for SW software (v3.1.8). Prior to running experimental samples, care was taken to
745 optimize the dilutions of lysates to be within the linear range of the detection.

746 **Coating of coverslips with different ECM proteins** #1.5 round glass coverslips (Electron
747 Microscopy Sciences. Catalog # 72230-01) were coated with the following ECM proteins when
748 noted: gelatin (Sigma Aldrich, catalog # G2500) (0.1% (w/v) of gelatin was prepared in Milli-Q
749 water and autoclaved to dissolve), vitronectin (Sigma Aldrich, catalog # SRP3186; stock
750 solution was prepared as 200µg/ml in 0.1% BSA and water) and laminin (R&D systems,
751 catalog # 3400-010-02, stock 1 mg/ml was pipetted into 10ul aliquots and stored at -80°C). To
752 coat with gelatin, glass surfaces were incubated with the 0.1% gelatin solution for 5 min at
753 room temperature (RT). To coat with vitronectin or laminin, glass surfaces were incubated at
754 37° C for 1 hr in 20 μg/ml of either vitronectin or laminin, excess liquid was removed, cover
755 slips were rinsed once with 1X PBS, and blocked with 10 μg/ml heat denatured BSA for 30 min
756 before plating cells (Lu et al., 2020).

757 **MEFs plated on different substrata** MEFs were grown either on #1.5 round glass coverslips
758 in 24-well dishes or in 8-well glass Ibidi dishes depending on the experiment for the times
759 indicated in figure legends. MEFs were then rinsed with 1X PBS (warmed to 37^0 C) for 5 min,
760 fixed with freshly thawed 4% PFA pre-warmed to 37^0 C for 20 min, and washed three times
761 with 1X PBS (warmed to 37^0 C) with mild shaking. All subsequent washing steps were done
762 with shaking. For permeabilization, cells were washed once in 1X PBS containing 0.1% Triton-
763 X 100 (PBST). Blocking was done for 30 min in 10% Donkey serum prepared in PBST
764 (blocking solution). After blocking, cells were incubated in primary antibodies diluted in
765 blocking solution overnight at 4^0 C, as specified in **Table M2**. This was followed by 3 washes in
766 PBST for 10 min each. Cells were then incubated with secondary antibodies diluted in PBST
767 for 60 min at RT. Finally, cells were washed three times with PBST for 10 min each. DAPI
768 (1:300) was added to the second wash. Cells were mounted using Vectashield.
769

770 **Hydrogels**

771 **Methacrylated Alginate Synthesis:** Methacrylated alginate (MeAlg) was synthesized
772 according to a previously established protocol (Khetan et al., 2013). In brief, alginic acid sodium
773 salt from brown algae (Sigma-Aldrich, USA) (3% w/v) was fully dissolved in Dulbecco's
774 phosphate buffered saline (dPBS, Sigma-Aldrich, USA). Then, methacrylic anhydride (Sigma-
775 Aldrich, USA) (8% v/v) was added drop-wise to the alginate solution and stirred for 12 h at 4^oC,
776 using 2M NaOH (Sigma-Aldrich, USA) to ensure that the pH remained between 8 and 9 for the
777 duration of the reaction. The resulting solution was passed through filter paper (GE Whatman)
778 and poured into Spectra/Por dialysis membrane with a 6–8 kDa molecular weight cutoff (Fischer
779 Scientific) and kept in DIW under stirring for 7 days to eliminate the unreacted MA and salts.
780 Dialyzed solution was then freeze-dried for 4 days to obtain MeAlg foam.

781 **Fabrication of the Hydrogel Substrates:** MeAlg substrates were fabricated using a previously
782 established protocol (Guvendiren and Burdick, 2012). Briefly, petri dishes with glass bottoms
783 were treated with UV/ozone (UVO) for 30 minutes, immediately followed by a coating of 3-
784 (trimethoxysilyl)propyl methacrylate (TMS) (Sigma-Aldrich, USA) to methacrylate the glass
785 surfaces (Guvendiren et al., 2009). The dishes were left in a desiccator overnight. The hydrogels
786 were fabricated using Michael-type addition polymerization. First, 2-hydroxy-4'-(2-
787 hydroxyethoxy)-2-methylpropiophenone (I2959) (Sigma-Aldrich, USA), a photoinitiatior (0.5%
788 w/v) was completely dissolved in Dulbecco's PBS (dPBS), followed by the lyophilized MeAlg (3%
789 w/v) synthesized previously. This was kept at room temperature until a clear solution was
790 achieved. Crosslinking occurs with the introduction of DL-Dithiothreitol (DTT) (Sigma-Aldrich,
791 USA) to the solution, along with 0.2M triethanolamine (Sigma-Aldrich, USA) at pH 10. To form
792 3kPa and 12 kPa gels, 20% and 30% (w/v) DTT are used, respectively. To promote cell
793 adhesion, GRGDSPC peptide (1% w/v) (Genscript) was added to the solution. After all contents
794 were thoroughly mixed, 5μL of MeAlg solution was pipetted onto the surface of the dish before
795 being covered with a glass coverslip in order to create gels less than 30μm thick. These were
796 left at room temperature for an hour to crosslink before being submerged in dPBS to remove the
797 coverslip.

798 **Atomic Force Microscopy** For stiffness measurements, hydrogel samples were submerged in
799 PBS and placed in a Dimension Icon AFM with ScanAsyst (Bruker). Using the PeakForce-QNM
800 mode, hydrogel samples were indented using an MLCT-Bio probe tip with pyramidal geometry
801 (Bruker, CA) and a nominal spring constant of 0.03 N/m, checked by thermal calibration.
802

803 **Treatment of cells with Deoxycholate (DOC)** 10^4 Fn1$^{mEGFP/+}$ MEFs were plated for 48 hrs in
804 8-well glass bottom Ibidi dishes in complete medium and incubated at 37° C and 5% CO_2. Two
805 hours before imaging SiR-actin was added at 1 μM final concentration. SiR-actin contains a

806 far-red dye, silicon rhodamine, conjugated to jasplakinolide that labels F-actin in live and fixed
807 cells (Lukinavicius et al., 2014). Just before imaging, complete medium was replaced by 150 μl
808 imaging medium containing 33 μg/ml of Hoechst 33342. Positions were marked in each well
809 and live imaging was initiated at 37°C and 5 % CO_2 humidified chamber. After 15 min, 150 μl
810 4% DOC solution prepared in imaging medium containing 33 μg/ml Hoechst was added to the
811 experimental well (final pH 8.01) and 150 μl imaging medium containing 33 μg/ml Hoechst but
812 without DOC was added to the control well. Cells were imaged at 50 sec intervals until F-actin
813 and DNA disappeared (see Movie 4). The medium was then removed, cells were rinsed for 1
814 min with 1X PBS pre-warmed to 37°C, fixed with 4% PFA pre-warmed to 37°C. For staining,
815 cells were permeabilized and blocked as above, and then incubated with Abcam monoclonal
816 anti-Fn1 antibody diluted 1:300 dilution in the blocking solution at 4°C overnight. Primary
817 antibodies were detected with anti-rabbit secondary antibodies conjugated to AlexaFluor647.
818 Enhanced-resolution imaging was used to image the DOC-treated fibrils, as described below.

819 **Confocal settings for enhanced resolution imaging** Confocal images of fixed samples were
820 recorded using Nikon A1-HD25 inverted confocal microscope equipped with CFI
821 Apochromat TIRF 100xC Oil objective with the pinhole set to 0.8 Airy units, and imaged
822 through 2 – 4 microns with step size of 0.125 μm - 0.15 μm at a sampling of 40 nm per pixel
823 and 180 nm optical resolution. Deconvolution was done using Nikon 3D deconvolution
824 software (v5.11.01). Airyscan imaging was performed using Zeiss LSM 880 fitted with a 32
825 array AiryScan GaAsP-PMT detector and the Plan Apochromat 63X Oil (NA 1.4) objective.
826 Deconvolution and pixel reassignment were done using Zeiss LSM software.
827

828 **Quantification of effective labeling efficiency and the number of Fn1 molecules in Fn1**
829 **nanodomains.** To quantify the number of Fn1 molecules per nanodomain and to measure
830 effective labeling efficiency, we used Nup96-mEGFP U2OS cells as a reference cell line and

831 SMAP software (Ries, 2020; Thevathasan et al., 2019). In Nup96-mEGFP cells, two copies of
832 the nucleoporin Nup96 gene are tagged with the monomeric enhanced green fluorescent
833 protein (mEGFP) at the C-terminus of the Nup96 gene, generating Nup96-mEGFP fusion
834 protein (Thevathasan et al., 2019). The stoichiometry of Nup96-mEGFP in nucleopores is well
835 characterized, and careful measurements, imaging methodology, and software have been
836 developed (Diekmann et al., 2020; Ries, 2020; Thevathasan et al., 2019). Together, these
837 tools allow the use of Nup96-mEGFP cell line as a reference to assess the quality of SMLM
838 imaging protocol, measure effective labeling efficiency, and determine the number of Fn1-
839 mEGFP molecules in Fn1 nanodomains.
840
841 Nup96-mEGFP cells (clone #195, Cell Line Services, CLS, clsgmbh.de, catalogue no. 300174)
842 were cultured according to the vendor's specifications in McCoy's 5a medium. Fn1-mEGFP
843 MEFs were cultured in complete DMEM as described above. $3x10^5$ Nup96-mEGFP cells and
844 $5x10^4$ Fn1-mEGFP cells were plated in their specified culture medium on 25 mm high precision
845 glass cover slips #1.5H (Marienfeld ref# 0117650, obtained from Azer Scientific, PA, USA, cat
846 # ES0117650) positioned in 6-well plates (Corning, cat # 353046). Prior to their use, glass
847 cover slips were cleaned using concentrated nitric acid, washed in water, and autoclaved, as
848 described in (Kaech and Banker, 2006). Coverslips were used without coating. 24 hours after
849 plating, cells were fixed and stained as described in (Thevathasan et al., 2019) with minor
850 modifications. Cover slips with Nup96-mEGFP cells and Fn1-mEGFP cells were handled
851 contemporaneously in pairs at each step. For fixation, permeabilization and washing,
852 coverslips were kept in 6-well plates. Cells were fixed in PBS containing 2.4% PFA for 20 min
853 at RT. PFA was aspirated and cells were incubated with 100mM NH_4Cl in PBS for 5 min at RT,
854 and then washed 3 x 5 min in PBS with agitation. Cells were permeabilized for 20 min at RT
855 using PBS containing either 0.2% Triton-X for Nup96-mEGFP cells or 0.1% Triton-X for Fn1-
856 mEGFP. Cells were then washed in PBS 3 x 5 min at RT, and washed once more for 5 min in

857 PBS containing 0.1% Triton-X, and then either used immediately for staining, or stored at 4°C
858 in PBS containing 0.1% Triton-X (PBST) until further use. For each experiment, sufficient
859 amounts of each solution were prepared such that Nup96- mEGFP and Fn1-mEGFP cells
860 were incubated with the same mixtures. Solutions containing blocking reagents and antibodies
861 were spun for 5 min at top speed using tabletop centrifuges to get rid of particulates.
862 Humidified chambers were prepared from empty pipet tip boxes with water placed in the lower
863 chamber and parafilm partially covering the surface of the tip rack. Drops of solutions were
864 placed on the parafilm, and cells were incubated with various solutions by inverting coverslips
865 on top of the droplets. To block non-specific antibody binding, cells were first incubated with a
866 blocking solution (10% donkey serum in PBST) for 30 min at RT. Cover slips were then gently
867 lifted, drained, and incubated with anti-GFP antibody (Aves lab, cat# GFP-1010) diluted 1:100
868 in the blocking solution overnight at 4°C. Coverslips were then placed into 6-well plates and
869 washed 3 x 5 min in PBST with agitation. Cells were then incubated with Alexa-647-conjugated
870 anti-chicken F(ab)$_2$ (Jackson ImmunoResearch 703-606-155) diluted 1:300 in the blocking
871 solution for 4 hours at RT, and then washed 3 x 5 min in PBST with agitation. Stained
872 coverslips were stored at 4°C until imaging.
873
874 **Preparation of cover slips for SMLM imaging** Coverslips with plated cells were rinsed with
875 GLOX/BME buffer and mounted onto single cavity glass slides (VWR, cat #10118-600), pre-
876 filled with 80 μl GLOX/BME buffer immediately prior to the placement of coverslip. Excess
877 buffer was fully adsorbed from the sides and the top of the coverslip with Whatman paper,
878 taking care to keep the coverslip centered on top of the cavity. Coverslips were sealed onto the
879 cavity slide by pipetting Acid-Free Elmer's No-Wrinkle Rubber Cement (Amazon.com,
880 https://www.amazon.com/Elmers-No-Wrinkle-Rubber-Cement-Acid-
881 Free/dp/B014JUDMBA/ref=sr_1_2?keywords=Elmer%27s+No-

882 Wrinkle+Rubber+Cement%2C+Acid-Free&qid=1637633240&sr=8-2) around the edge, and
883 allowing the rubber cement to cure for ~15 min. After imaging, rubber cement was gently
884 peeled off, and the slides were soaked in PBST for 5 min at RT to remove cover slips which
885 were then stored in 6-well plates filed with PBST containing 0.02% NaN_3 at 4°C until further
886 use. In this set up, the GLOX/BME buffer remained at pH 8 for at least 12 hours.
887
888 **SMLM Imaging protocol to quantify the effective labeling efficiency and the number of**
889 **mEGFP molecules in Fn1-mEGFP nanodomains.** For the following experiments, 2D imaging
890 was used to maximize the resolution in the plane of imaging. To minimize fluorophore
891 bleaching and maximize the number of collected photons we followed the protocol protocol
892 developed by (Diekmann et al., 2020). Stained Nup96-mEGFP and Fn1-mEGFP cells were
893 imaged in pairs using the same preparation of the GLOX/BME buffer and the same imaging
894 conditions (described below). For each independent experiment (n=4) and for each round of
895 measurements, images of Nup96-mEGFP and Fn1-mEGFP cells taken on the same day were
896 analyzed. SMLM was performed using Nikon A1-HD25 Ti2E microscope equipped with
897 motorized TIRF illumination, 125mW 640 nm solid-state laser, Perfect Focus, and CFI
898 Apochromat TIRF 100xC Oil objective with numerical aperture 1.49 (cat # MRD01905). All
899 images were acquired at the critical angle of incidence (57°) and recorded using a 512 x 512
900 EMCCD camera (Princeton Instruments), using 128 x 128 central region on the camera. Gain
901 was set to 3, multiplication gain amplifier was set to 20 MHz. Prior to acquisition, the centered
902 ROI (128 x 128) was bleached at 57° angle, and 10% laser power for 500 frames followed by
903 additional 500 frames at 20% laser power, with the exposure of 60 ms per frame. Images were
904 then acquired at 57° angle, 20% laser power, for 60,000 frames at 60 ms per frame. Images
905 were processed, rendered, and quantified using SMAP and Matlab version 2020a (Ries,
906 2020), as described (Diekmann et al., 2020) and the documentation found on
907 https://github.com/jries/SMAP. Settings for peak finding in the SMAP software were set

908 according to our camera's manufacture's specifications and were the following: EM was set to
909 "on", camera pixel size was set to 0.162 μm, EM gain was set to 300, e-/ADU conversion factor
910 was set to 2.35. Data was fitted using a Gaussian PSF model, the cutoff parameter for peak
911 finding was set to 2, and ROI size was set to 7 pixels. Localizations were then grouped and
912 rendered, using default parameters in SMAP. Drift correction was performed on rendered
913 localizations in timepoint blocks of 10 or 20, as recommended (Thevathasan et al., 2019) and
914 https://github.com/jries/SMAP. Following satisfactory drift correction judged by the overlapping
915 cross-correlations, localizations were filtered according to the recommended settings for Alexa-
916 647 fluorophore (Thevathasan et al., 2019), in brief, localizations with poor precision were
917 filtered out by limiting localization precision to 0 – 15 nm, out-of-focus localizations were
918 excluded by setting the PSF range to 0 – 150 nm in the x-y plane, poorly fitted localizations
919 were further filtered out by setting the LLrel parameter (relative log-likelihood) in SMAP to a
920 negative cut-off value leaving the majority of the peak intact, and the first 1000 frames were
921 excluded from the analyses. All the remaining grouped localization were rendered according to
922 $\sqrt{photons}$ and images were color-coded using LUTs set according to localization density.
923
924 Image resolution was measured using the Fourier Ring Correlation (FRC) method described
925 by (Nieuwenhuizen et al., 2013) and implemented in SMAP. Voronoi cluster discovery was
926 performed according to (Andronov et al., 2016a) and their algorithm implemented in SMAP.
927 DBSCAN cluster analysis was performed according to (Caetano et al., 2015; Ester et al., 1996)
928 implemented in SMAP; For DBSCAN, the minimum number of points in the neighborhood (k)
929 was set to 4, as recommended for all 2-dimentional data (Ester et al., 1996). The
930 neighborhood radius ε was set either to 14 nm (the average apparent radius of Fn1
931 nanodomains determined as described below) or automatically estimated by the DBSCAN
932 algorithm in SMAP (Ries, 2020).

933

934 NPC radius, effective labeling efficiency and the number of gourped localizations per
935 fluorophore were determined using the algorithm in SMAP following the published automated
936 workflow to segment and analyze nucleopore complexes (NPCs), using the parameters
937 recommended by (Thevathasan et al., 2019) without modifications. In brief, NPCs in focus
938 (mean fitted PFS size of each NPC was less then 145 nm) were automatically segmented
939 using circular ROI of 220 nm in diameter. The number of grouped localizations per NPC, NPC
940 radius, and effective labeling efficiency (ELE) were determined using published algorithms
941 implemented in SMAP without modifications, as described in (Diekmann et al., 2020;
942 Thevathasan et al., 2019) and the SMAP user manual "Analysis of NPCs using SMAP". Since
943 we used identical staining, imaging, and processing parameters for Nup96-mEGFP and Fn1-
944 mEGFP cells, the number of Fn1-mEGFP molecules per nanodomain was calibrated to the
945 number of grouped localizations per NUP96-mEGFP protein, as described (Thevathasan et al.,
946 2019). In brief, we first determined the number of merged localizations per NPC in the ROI
947 (L_{ref}). Each NPC contains 32 NUP96-mEGFP proteins, therefore, the number of merged
948 localizations per Nup96-mEGFP (N_{ref}) is $N_{ref}= L_{ref}/32$. To determine the number of Fn1-mEGFP
949 proteins per Fn1 nanodomain, we segmented Fn1 nanodomains manually using a circular ROI
950 of 60 nm in diameter and the number of merged localizations per ROI (L_t) was determined by
951 using the *countingStatistics plugin* in SMAP, as outlined in the SMAP manual "Analysis of
952 NPCs using SMAP". The number of Fn1-mEGFP proteins per nanodomains (N_t) is L_t / N_{ref}.
953 Since Fn1 is only secreted as a dimer, the number of Fn1 dimers per nanodomain is N_t /2.
954

955 Nanodomain periodicity in Fn1 fibrils stained by a variety of different antibodies was assayed
956 and quantified according to (Fruh et al., 2015). In brief, MEFs were stained using a variety of
957 antibodies at different dilutions, or using combinations of antibodies, as noted in **Figs. 5, 6, 8**,
958 according to the staining protocol described above and imaged using GLOX/BME buffer and

959 the exact imaging settings as described for imaging Nup96-mEGFP and Fn1-mEGFP cells
960 stained with anti-GFP antibodies (see above). Images were processed and rendered in SMAP
961 according to the parameters described above. Gaussian rendering of the localizations (min σ
962 Gaussian was set to 3nm) were saved as uncompressed tiff files and opened in Fiji version
963 2.1.0/1.53c, intensity line profiles along each fibril were generated and imported into Matlab
964 2021a. To assay the periodicity, we used the autocorrelation function implemented in the
965 Matlab's 2021a Econometrics toolbox and the criteria outlined in (Fruh et al., 2015). In brief,
966 the presence of at least four regularly-spaced peaks in the autocorrelation profile was
967 considered to reflect the periodical nature of Fn1 nanodomains, and the position of the first
968 autocorrelation maximum was taken as a quantitative measure of nanodomain periodicity, as
969 extensively discussed and computationally modelled in the Supplemental Data section of (Fruh
970 et al., 2015). Ljung-Box Q-test for residual autocorrelation was performed using Matlab's
971 2021a Econometrics toolbox to assess statistical significance of autocorrelation.
972 To determine the apparent diameter of Fn1 nanodomains, we imported fibril intensity
973 line profiles obtained from SMLM images of $Fn1^{mEGFP/mEGFP}$ MEFs stained for GFP into Matlab
974 2021a. To automate the analyses, we used Signal Processing toolbox in Matlab 2021a to fit
975 each intensity peak in the line profile with a Gaussian curve and calculate full width at half
976 height (FWHT) for each peak. Altogether, 1292 nanodomains in 27 long (> 1 μm in length)
977 fibrils from six cells and 3 independent experiments were assessed. We have also performed
978 this analysis manually on a subset of Fn1 nanodomains (n=248) in long fibrils by fitting a
979 Gaussian to an intensity profile of each individual nanodomain and calculating FWHT. The
980 results were the same.
981
982 **Assembly of exogenously-added Fn1: Part I, Live Imaging** 3-well culture insert (Ibidi, cat #
983 80366) was placed in the middle of the 35 mm glass-bottom dish (Ibidi, cat # 81158) and then

984 0.8 x 10^6 Fn1-tdTomato-expressing MEFs were plated surrounding the inserts and cultured for
985 24 hours to reach confluency and establish Fn1-tdTomato matrix. At a 24-hour time point, Fn1-
986 mEGFP-expressing MEFs were plated inside the inserts on glass without coating for 5 hours.
987 Prior to imaging, the culture medium was removed and replaced with the imaging medium.
988 Live imaging was performed using Plan Fluor 40x Oil (numerical aperture 1.3). Positions
989 containing Fn1-mEGFP-expressing MEFs were imaged at ~17-18 min intervals for ~16 hours
990 in humidified Tokai Hit stage-top incubator at 5% CO_2. Each position was imaged 40-43
991 confocal slices at 0.5 μm thickness, the pinhole was set to 1 Airy unit.
992
993 **Assembly of exogenously-added Fn1: Part II, SMLM** The medium containing secreted Fn1-
994 tdTomato fusion proteins was collected after a 72-hour culture of confluent Fn1-tdTomato
995 MEFs generated by CRISPR/Cas9 mutagenesis, as described above. The medium was spun
996 at 300 x *g* for 5 min to pellet debris. The concentration of Fn1-tdTomato in the supernatant was
997 quantified using ELISA kit using antibodies specific to mouse Fn1, which does not cross react
998 with bovine Fn1 (Abcam, cat # ab21097). Fn1-tdTomato-containing supernatant was diluted 4-
999 fold with fresh MEF culture medium to the final concentration of 5 μg/ml of Fn1-tdTomato, and
1000 2 ml of this supernatant were added to Fn1-mEGFP MEFs plated on 25 mm 1.5H glass
1001 coverslips the day before at 10^5 cells per well in a 6-well plate. Following 24-hours of
1002 incubation at 37°C and 5% CO_2, cells were washed with PBS and fixed in 4% PFA in PBS for
1003 20 min at RT. PFA was quenched with 100mM NH_4Cl in PBS, cell were washed 3x5 min in
1004 PBS, and permeabilized with PBS containing 0.1% Triton-X (PBST). Cells were then incubated
1005 with a blocking solution containing 10% donkey serum in PBST for 30 min at RT. To detect
1006 Fn1-tdTomato, cells were incubated at 4°C overnight with rabbit anti-mCherry antibody
1007 (Abcam, cat #ab167453) diluted 1:100 in the blocking solution. Primary antibodies were
1008 detected with Alexa-647-conjugated donkey anti-rabbit $F(ab)_2$ secondary antibodies (Jackson

1009 laboratories, cat # 711-606-152) diluted 1:300 in blocking solution and incubated for 4 hrs at
1010 RT. Cells were then washed 3x5min in PBST and stored at 4°C until imaging. dSTORM
1011 imaging was performed using GLOX/BME buffer. Cell were imaged at 57° angle using the
1012 SMLM imaging protocol, as described above. Images were processed and reconstructed using
1013 SMAP using the same parameters, as described above.
1014
1015 **Live imaging using TIRF** Fn1$^{mEGFP/+}$ MEFs were plated on 35-mm round glass bottom Mattek
1016 dishes (catalog # P35G-1.5-14-C), complete medium was switched to imaging medium prior to
1017 filming. Live TIRF microscopy was performed using Nikon A1-HD25 inverted confocal
1018 microscope equipped with 4 laser lines of 100mW per line at 405, 488, and 561nm and
1019 125mW at 640nm, and motorized TIRF illumination. CFI Apochromat TIRF 100xC Oil objective
1020 and EMCCD camera were used. Before imaging lasers were aligned and the critical angle of
1021 incidence for imaging was determined by the software. The exposure time was 20 ms and
1022 readout speed was set at 10 MHz.
1023
1024 **Live imaging using confocal point-scanning** Live cell imaging was performed using Ibidi
1025 glass bottom 8-well chambers (catalog # 80827). $0.6*10^4$ wild-type or Fn1$^{mEGFP/+}$ MEFs were
1026 plated on glass in each well of Ibidi glass bottom 8-well chambers and allowed to grow
1027 overnight prior to staining and imaging by direct Stochastic Optical Reconstruction Microscopy
1028 (dSTORM). For FUD and III-11C treatment, Fn1$^{mEGFP/+}$ MEFs were plated in 8-well glass Ibidi
1029 dishes (1 cm^2 growth area) without coating at a density of $0.6x10^4$ cells/well in complete
1030 medium. After 5 hours, DMEM was removed and cells were rinsed once with 1X PBS.
1031 Subsequently, the medium was changed to imaging medium. For FUD experiments, imaging
1032 medium was supplemented either with 225 nM FUD or 274 nM of control III-11C peptide.
1033 Untreated wells contained cells incubated with imaging medium. Following the addition of the
1034 imaging medium (with or without the peptides), the chamber was immediately set up for

1035 imaging in the humidified Tokai Hit stage-top incubator at 37°C, 5% CO_2. Live imaging was
1036 performed using Nikon A1-HD25 inverted confocal microscope with the DUG 4-Channel
1037 Detector and 2 GaAsP, 2 high-sensitivity PMTs, and a motorized XYZ stage with Nikon's
1038 Perfect Focus 4 system, and Plan Fluor 40x Oil (numerical aperture 1.3, cat # MRH01401).
1039 mEGFP was excited using 488 nm laser at 1% power and pinhole set to 1 Airy unit. An optical
1040 zoom of 2 and Z step size of 0.5 μm were used, and stack size was set to 10-15 microns
1041 allowing to image the entire cell. For overnight movies, each position was filmed every 1.5 min
1042 – 4 min, as noted in Movie legends. Movies in the mp4 format were generated using Imaris
1043 9.5.1 (Bitplane), titles and arrows were added using Adobe Premiere Elements Editor 2020.
1044
1045 **SMLM imaging protocol used to image cells plated on Ibidi glass-bottom dishes.** This
1046 protocol was used to image cells following the live DOC assay or overnight live imaging (**Fig.**
1047 **10** and **Sup. Fig. 9**). Following fixation with 4% PFA, cells were washed with PBS, incubated
1048 with blocking buffer containing PBS, 0.1% Triton-X, and 10% donkey serum for 30 min at RT.
1049 Cells were then incubated with Abcam monoclonal anti-Fn1 antibody diluted at 1:300 in
1050 blocking buffer overnight at 4°C. Following three washes at 5 min each in PBST (PBS with
1051 0.1% TritonX), cells were incubated with Alexa-647-conjugated anti-rabbit secondary
1052 antibodies diluted 1:300 in blocking buffer for 4 hours at RT, and washed three washes at 5
1053 min each in PBST. Prior to imaging, freshly prepared GLOX/MEA buffer was added and the
1054 chamber was immediately sealed using parafilm. STORM was performed using Nikon A1-
1055 HD25 Ti2E microscope equipped with motorized TIRF illumination, 125mW 640 nm solid-state
1056 laser, Perfect Focus, and a 100x/1.49NA objective. Images were acquired at the critical angle
1057 of incidence and recorded using a 512 x 512 EMCCD camera (Princeton Instruments).
1058 Calibration was obtained by imaging of 100 nm Tetraspeck beads (Life technologies, catalog #
1059 T-7279) using the same glass surface and buffer conditions. To drive Alexa-647 into the dark

1060 state, samples were pre-bleached by the illumination at 640 nm for 10 seconds at 100 % laser
1061 power. 40,000 frames were acquired at 8.4 ms exposure. Blinking events were fitted using the
1062 Nikon N-STORM localization software. Images were analyzed using Nikon software (Nikon
1063 Elements AR Software v5.11.01). Localization events with fewer than 800 or more than 50000
1064 photons were filtered out to remove blinking evens that were either too faint or too bright. In
1065 addition, blinking events were filtered out if they occurred in more than 5 consecutive frames or
1066 where outside the z-range determined by the calibration using 100 nm Tetraspeck beads.
1067 Images in which z-rejection was below 50% were used for further analyses.
1068
1069 **Analysis of localization numbers in fibrillar and non-fibrillar nanodomains** In order to
1070 enrich for non-fibrillar nanodomains, Fn1$^{mEGFP/+}$ MEFs were plated in 8 well glass Ibidi dishes
1071 (1 cm^2 growth area) without coating. Cell were plated at the density of $0.6x10^4$ cells/well in
1072 imaging medium with or without FUD (225 nM) or III-11C (274 nM), and incubated in at 37°C,
1073 5% CO_2 for 1 hr. Subsequently, MEFs were rinsed once in warm 1X PBS and fixed using pre-
1074 warmed 4% PFA for 20 min. After fixation, wells were rinsed three times, 5 min each with Stain
1075 Buffer (cat # 554656 BD Pharmingen), blocked for 30 min at room using 5% Donkey serum
1076 prepared in Stain Buffer, and incubated with the monoclonal anti-Fn1 (Abcam, cat # 199056)
1077 overnight at 4° C. Cell were then washed with Stain Buffer three times, 10 min each, and
1078 incubated with anti-rabbit antibodies conjugated with Alexa-647 for 1 hour at rt. Cell were then
1079 rinsed again with Stain Buffer three times, 10 min each, and stored at 4° C in 1X PBS. STORM
1080 imaging was performed, as above. To quantify the number of grouped localizations per
1081 nanodomain, we used the free-hand ROI tool in the STORM window (Nikon Elements AR
1082 Software v5.11.01) to determine the number of localizations within non-fibrillar and fibrillar Fn1
1083 nanodomains. Fn1 nanodomains were analyzed in 5 random regions from 3 independently
1084 acquired images (a total of 15 fields) for each sample. To determine the number of
1085 localizations in Fn1 nanodomains within fibrils, we analyzed more than 20 from 3 or more

1086 independently acquired images. All the counts were plotted in Prism 8.2.1 (GraphPad
1087 Software, USA), and compared using either one-way ANOVA test with Tukey's correction or
1088 Kruskal-Wallis test with Dunn's correction for multiple testing.
1089
1090 **Double-color dSTORM acquisition** Samples were mounted with the SMART Kit buffer
1091 (Abbelight). 2D or 3D STORM images were acquired using a SAFe360 module (Abbelight)
1092 coupled to an inverted bright-field Olympus IX83 microscope, equipped with a 100X oil-
1093 immersion objective (1.49 NA). This dual-cam system (sCMOS cameras, Orcaflashv4,
1094 Hamamatsu) allows to perform multicolor STORM by spectral demixing strategy coupled to the
1095 use of far-red dyes (BioOptics World, 2021, Caorsi and Karlsson).
1096 Briefly, a dichroic at 700nm is used to separate the fluorescence emission from AF647 and
1097 CF680 dyes. The Point Spread Function (PSF) of each detection can be retrieved on both
1098 cameras and the measured photon numbers is related to the spectral separation of the

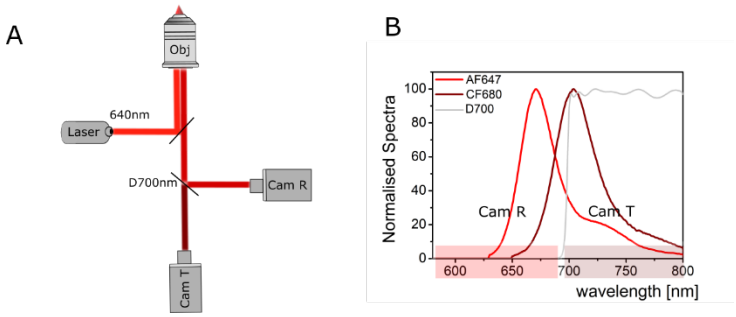

Figure M1. Spectral de-mixing optical scheme. A. A 640 nm laser is sent through the objective lens to excite AF647 and CF680 fluorophores. The emitted light is separated by a 700 nm long pass dichroic filter that reflects light below 700 nm into the Reflected camera (Cam R) and transmits light above 700 nm into the Transmitted camera (Cam T). **B.** Emission spectra of AF647 and CF680 dyes together with a 700nm dichroic filter showing spectral separation into the two cameras Cam R and Cam T.

1099 fluorophore (**Fig. M1**).
1100
1101
1102
1103

Typically, acquisition of 60000 frames at 20ms exposure time on a camera sensor size of 1024x1024 pixel were acquired to collect single-molecule detections. The irradiation at the sample could be properly tuned thanks to ASTER technology (Mau et al. 2021 Nature Communications, https://www.nature.com/articles/s41467-021-23405-4) implemented on the SAFe360 Abbelight module. Resulting coordinate tables and images were processed and analyzed using NEO software (Abbelight).

As the PSF is captured on both cameras, transmitted and reflected, a ratiometric analysis is applied: a ratio for each detection is calculated and the final ratio distribution is used for lambda assignment:

$$R_{A,i} = \frac{I_{R,i}}{I_{R,i} + I_{T,i}}$$

where the suffix A is the fluorophore, i the localisation and I_R and I_T the intensity measured on camera R and camera T (i.e. the number of photons emitted per molecule).

1121 Average ratio distributions obtained from measurements are shown in **Fig.M2**:

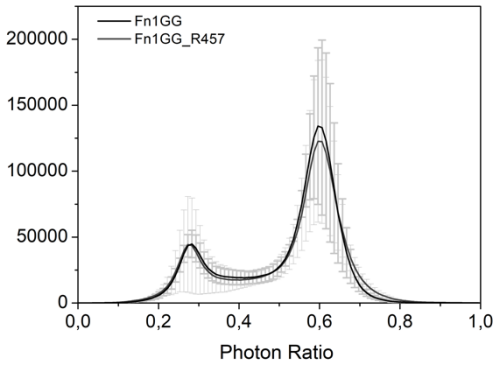

Figure M2. Average ratio distributions for Fn1$^{mEGFP/mEGFP}$ cells stained using chicken anti-GFP and rabbit anti-GFP antibodies (Fn1GG, dark gray) or chicken anti-GFP and rabbit R457 antibodies (Fn1GG_R457, lighter gray). The two fluorophore populations can be clearly distinguished for lambda assignment.

1122
1123
1124 Following the ratio distributions measured on the samples the following parameters have been
1125 used for separation: detections with ratios between 0-0.45 were assigned to CF680 and
1126 detections with ratios between 0.5-1 were assigned to AF647. On average 3% of detections
1127 were rejected while keeping crosstalk below 1%. Following de-mixing, colocalization analysis
1128 was performed on Neo software following the CBC algorithm (Malkusch et al., 2012).
1129 Parameters set for CBC analysis were R_{max} at 300 nm and a number of steps equal to 10.

1130

1131 **Legends for Movies**

1132 **Movie 1. Rotational views through the Fn1+ ECM in the cardiac jelly.** The whole E9.5
1133 embryo was stained using Abcam rabbit monoclonal anti-Fn1 antibody and imaged using 100x
1134 objective, N.A. 1.49, with the pinhole set at 0.8 Airy units, and sampling of 40 nm per pixel in x,
1135 y. The movie shows 3D reconstruction through 3.4 μm of tissue sampled every 0.121 μm in z.
1136 Fn1 is in white, DAPI is in blue. Arrows point to examples of beaded Fn1 fibrils.

1137

1138 **Movie 2. Fn1 fibrillogenesis imaged by TIRF microscopy.** Fn1^{mEGFP} MEFs were transiently
1139 transfected with mCardinal-Lifeact, plated on gelatin-coated glass coverslips, and imaged 48
1140 hours later. Filming was done every 2 min for 30 min using TIRF and 100x objective, N.A.
1141 1.49. The first set shows the Fn1-mEGFP channel. Yellow arrows point to centripetally-moving
1142 Fn1 nanodomains organized into an elongating linear fibril. The second set is an overlay
1143 between Fn1-mEGFP and mCardinal-Lifeact.
1144
1145 **Movie 3. 2% DOC dissolved cytoplasm and nucleus in under 13 min leaving Fn1 fibrils.**
1146 MEFs expressing Fn1-mNeonGreen were plated on glass-bottom slides without coating and
1147 labeled with SiRActin (magenta) to visualize F-actin, and Hoechst (blue) to visualize DNA.
1148 Time-lapse was recorded every 54 sec immediately following the addition of the DOC solution
1149 pH 8.01 to live cells. The presence of 2% DOC dissolves actin cytoskeleton and nuclei and
1150 leaves Fn1 ECM fibrils (green). Fn1 fibrils collapse following the dissolution of the actin
1151 cytoskeleton due to the loss of tension.
1152
1153 **Movie 4. Fibrillogenesis of ectopic Fn1.** 3-well culture insert was placed in the middle of the
1154 35 mm glass-bottom dish and 0.8 x 10^6 Fn1-tdTomato-expressing MEFs were plated
1155 surrounding the inserts. 24 hours later, Fn1-mEGFP-expressing MEFs were plated inside the
1156 inserts on glass without coating for 5 hours. Confocal live imaging of areas containing Fn1-
1157 mEGFP-expressing MEFs was performed using Plan Fluor 40x Oil (NA 1.3). Positions
1158 containing Fn1-mEGFP-expressing MEFs were imaged at 17-18 min intervals for ~16 hours.
1159 This movie contains maximum intensity projections composed of forty-three confocal slices at
1160 0.5 μm thickness, the pinhole was set to 1 Airy unit. The first still panel in this movie is a
1161 montage of the plate to show Fn1-tdTomato and Fn1-mEGFP-expressing cells prior to the start
1162 of the time-lapse.

1163

1164 **Movie 5. Cells incubated with 11-IIIC, show robust fibrillogenesis.** Fn1$^{mEGFP/+}$ MEFs were
1165 plated on uncoated glass in 8-well Ibidi chambers for 4 hours. Medium containing 11-IIIC
1166 control peptide was then added and cells were filmed every 90 sec for about 15 hours, as
1167 described in Methods. The movie begins approximately 30 min after the 11-IIIC-containing
1168 medium was added, the time it takes to set up time-lapse recording. Arrows point to the cell
1169 periphery and examples of centripetally moving Fn1 fibrils.

1170

1171 **Movie 6. FUD interferes with linking centripetally moving Fn1+ nanodomains into fibrils.**
1172 Fn1$^{mEGFP/+}$ MEFs were plated on glass in 8-well Ibidi chambers for 4 hours. Medium containing
1173 FUD peptide was then added and cells were filmed every 3 min for about 15 hours, as
1174 described in Methods. The movie begins approximately 30 min after the FUD-containing
1175 medium was added, the time it takes to set up time-lapse recording. Note the dismantling of
1176 pre-existing fibrils at the beginning of the movie. Yellow and red arrows point to the cell
1177 periphery. Note the presence of centripetally moving Fn1-mEGFP “beads” and the scarcity of
1178 Fn1 fibrils for the majority of the duration of the movie.

1179

1180 **References**

1181 Aguirre, K.M., R.J. McCormick, and J.E. Schwarzbauer. 1994. Fibronectin self-association is
1182 mediated by complementary sites within the amino-terminal one-third of the molecule. *J Biol*
1183 *Chem*. 269:27863-27868.

1184 Andronov, L., Y. Lutz, J.L. Vonesch, and B.P. Klaholz. 2016a. SharpViSu: integrated analysis
1185 and segmentation of super-resolution microscopy data. *Bioinformatics*. 32:2239-2241.

1186 Andronov, L., I. Orlov, Y. Lutz, J.L. Vonesch, and B.P. Klaholz. 2016b. ClusterViSu, a method
1187 for clustering of protein complexes by Voronoi tessellation in super-resolution microscopy. *Sci*
1188 *Rep*. 6:24084.

1189 Arai, Y., R. Yasuda, K. Akashi, Y. Harada, H. Miyata, K. Kinosita, Jr., and H. Itoh. 1999. Tying
1190 a molecular knot with optical tweezers. *Nature*. 399:446-448.

1191 Baumgart, F., A.M. Arnold, K. Leskovar, K. Staszek, M. Folser, J. Weghuber, H. Stockinger,
1192 and G.J. Schutz. 2016. Varying label density allows artifact-free analysis of membrane-protein
1193 nanoclusters. *Nat Methods*. 13:661-664.

1194 Behringer, R., M. Gertsenstein, K. Vintersten, and A. Nagy. 2014. Manipulating the Mouse
1195 Embryo: A Laboratory Manual. Cold Spring Harbor Laboratory Press, New York. 814 pp.

1196 Bui, K.H., A. von Appen, A.L. DiGuilio, A. Ori, L. Sparks, M.T. Mackmull, T. Bock, W. Hagen,
1197 A. Andres-Pons, J.S. Glavy, and M. Beck. 2013. Integrated structural analysis of the human
1198 nuclear pore complex scaffold. *Cell*. 155:1233-1243.

1199 Caetano, F.A., B.S. Dirk, J.H. Tam, P.C. Cavanagh, M. Goiko, S.S. Ferguson, S.H. Pasternak,
1200 J.D. Dikeakos, J.R. de Bruyn, and B. Heit. 2015. MIiSR: Molecular Interactions in Super-
1201 Resolution Imaging Enables the Analysis of Protein Interactions, Dynamics and Formation of
1202 Multi-protein Structures. *PLoS Comput Biol*. 11:e1004634.

1203 Chen, Y., L. Zardi, and D.M. Peters. 1997. High-resolution cryo-scanning electron microscopy
1204 study of the macromolecular structure of fibronectin fibrils. *Scanning*. 19:349-355.

1205 Chernousov, M.A., A.I. Faerman, M.G. Frid, O. Printseva, and V.E. Koteliansky. 1987.
1206 Monoclonal antibody to fibronectin which inhibits extracellular matrix assembly. *FEBS Lett*.
1207 217:124-128.

1208 Chiang, H.Y., V.A. Korshunov, A. Serour, F. Shi, and J. Sottile. 2009. Fibronectin is an
1209 important regulator of flow-induced vascular remodeling. *Arterioscler Thromb Vasc Biol*.
1210 29:1074-1079.

1211 Choi, M.G., and R.O. Hynes. 1979. Biosynthesis and processing of fibronectin in NIL.8
1212 hamster cells. *J Biol Chem*. 254:12050-12055.

1213 Diekmann, R., M. Kahnwald, A. Schoenit, J. Deschamps, U. Matti, and J. Ries. 2020.
1214 Optimizing imaging speed and excitation intensity for single-molecule localization microscopy.
1215 *Nat Methods*. 17:909-912.

1216 Dzamba, B.J., and D.M. Peters. 1991. Arrangement of cellular fibronectin in noncollagenous
1217 fibrils in human fibroblast cultures. *J Cell Sci*. 100 (Pt 3):605-612.

1218 Engel, J., E. Odermatt, A. Engel, J.A. Madri, H. Furthmayr, H. Rohde, and R. Timpl. 1981.
1219 Shapes, domain organizations and flexibility of laminin and fibronectin, two multifunctional
1220 proteins of the extracellular matrix. *J Mol Biol*. 150:97-120.

1221 Erickson, H.P., N. Carrell, and J. McDonagh. 1981. Fibronectin molecule visualized in electron
1222 microscopy: a long, thin, flexible strand. *J Cell Biol*. 91:673-678.

1223 Ester, M., H.-P. Krigel, J. Sander, and X. Xu. 1996. A density-based algorithm for discovering
1224 clusters in large spatial databases with noise. *Proc Second Int Conf Knowl Discov Data*
1225 *Min.*:226–231.

1226 Filla, M.S., K.D. Dimeo, T. Tong, and D.M. Peters. 2017. Disruption of fibronectin matrix affects
1227 type IV collagen, fibrillin and laminin deposition into extracellular matrix of human trabecular
1228 meshwork (HTM) cells. *Exp Eye Res*. 165:7-19.

1229 Fruh, S.M., I. Schoen, J. Ries, and V. Vogel. 2015. Molecular architecture of native fibronectin
1230 fibrils. *Nat Commun*. 6:7275.

1231 Furcht, L.T., D. Smith, G. Wendelschafer-Crabb, D.F. Mosher, and J.M. Foidart. 1980a.
1232 Fibronectin presence in native collagen fibrils of human fibroblasts: immunoperoxidase and
1233 immunoferritin localization. *J Histochem Cytochem*. 28:1319-1333.

1234 Furcht, L.T., G. Wendelschafer-Crabb, D.F. Mosher, and J.M. Foidart. 1980b. Ascorbate-
1235 induced fibroblast cell matrix: reaction of antibodies to procollagen I and III and fibronectin in
1236 an axial periodic fashion. *Prog Clin Biol Res*. 41:829-843.

1237 Furcht, L.T., G. Wendelschafer-Crabb, D.F. Mosher, and J.M. Foidart. 1980c. An axial periodic
1238 fibrillar arrangement of antigenic determinants for fibronectin and procollagen on ascorbate
1239 treated human fibroblasts. *J Supramol Struct*. 13:15-33.

1240 Geiger, B., A. Bershadsky, R. Pankov, and K.M. Yamada. 2001. Transmembrane crosstalk
1241 between the extracellular matrix--cytoskeleton crosstalk. *Nature reviews. Molecular cell*
1242 *biology*. 2:793-805.

1243 Geiger, B., and K.M. Yamada. 2011. Molecular architecture and function of matrix adhesions.
1244 *Cold Spring Harb Perspect Biol*. 3.

1245 Gudzenko, T., and C.M. Franz. 2015. Studying early stages of fibronectin fibrillogenesis in
1246 living cells by atomic force microscopy. *Mol Biol Cell*. 26:3190-3204.

1247 Guvendiren, M., and J.A. Burdick. 2012. Stiffening hydrogels to probe short- and long-term
1248 cellular responses to dynamic mechanics. *Nat Commun*. 3:792.

1249 Guvendiren, M., S. Yang, and J.A. Burdick. 2009. Swelling-Induced Surface Patterns in
1250 Hydrogels with Gradient Crosslinking Density. *Advanced Functional Materials*. 19:3038-3045.

1251 Heilemann, M., S. van de Linde, M. Schuttpelz, R. Kasper, B. Seefeldt, A. Mukherjee, P.
1252 Tinnefeld, and M. Sauer. 2008. Subdiffraction-resolution fluorescence imaging with
1253 conventional fluorescent probes. *Angew Chem Int Ed Engl*. 47:6172-6176.

1254 Hocking, D.C., J. Sottile, and P.J. McKeown-Longo. 1994. Fibronectin's III-1 module contains a
1255 conformation-dependent binding site for the amino-terminal region of fibronectin. *J Biol Chem*.
1256 269:19183-19187.

1257 Hynes, R.O. 1990. Fibronectins. Springer-Verlag, New York.

1258 Hynes, R.O. 2009. The extracellular matrix: not just pretty fibrils. *Science*. 326:1216-1219.

1259 Jimenez, A., K. Friedl, and C. Leterrier. 2020. About samples, giving examples: Optimized
1260 Single Molecule Localization Microscopy. *Methods*. 174:100-114.

1261 Kaech, S., and G. Banker. 2006. Culturing hippocampal neurons. *Nat Protoc*. 1:2406-2415.

1262 Khetan, S., M. Guvendiren, W.R. Legant, D.M. Cohen, C.S. Chen, and J.A. Burdick. 2013.
1263 Degradation-mediated cellular traction directs stem cell fate in covalently crosslinked three-
1264 dimensional hydrogels. *Nature Materials*. 12:458-465.

1265 Lansky, Z., Y. Mutsafi, L. Houben, T. Ilani, G. Armony, S.G. Wolf, and D. Fass. 2019. 3D
1266 mapping of native extracellular matrix reveals cellular responses to the microenvironment. *J*
1267 *Struct Biol X*. 1:100002.

1268 Lelek, M., M.T. Gyparaki, G. Beliu, F. Schueder, J. Griffié, S. Manley, R. Jungmann, M. Sauer,
1269 M. Lakadamyali, and C. Zimmer. 2021. Single-molecule localization microscopy. *Nature*
1270 *Reviews Methods Primers*. 1:39.

1271 Lu, J., A.D. Doyle, Y. Shinsato, S. Wang, M.A. Bodendorfer, M. Zheng, and K.M. Yamada.
1272 2020. Basement Membrane Regulates Fibronectin Organization Using Sliding Focal
1273 Adhesions Driven by a Contractile Winch. *Dev Cell*. 52:631-646 e634.

1274 Ma, W., H. Ma, and D.F. Mosher. 2015. On-Off Kinetics of Engagement of FNI Modules of
1275 Soluble Fibronectin by beta-Strand Addition. *PLoS One*. 10:e0124941.

1276 Malkusch, S., U. Endesfelder, J. Mondry, M. Gelleri, P.J. Verveer, and M. Heilemann. 2012.
1277 Coordinate-based colocalization analysis of single-molecule localization microscopy data.
1278 *Histochem Cell Biol*. 137:1-10.

1279 Martino, M.M., and J.A. Hubbell. 2010. The 12th-14th type III repeats of fibronectin function as
1280 a highly promiscuous growth factor-binding domain. *FASEB J*. 24:4711-4721.

1281 Maurer, L.M., B.R. Tomasini-Johansson, W. Ma, D.S. Annis, N.L. Eickstaedt, M.G.
1282 Ensenberger, K.A. Satyshur, and D.F. Mosher. 2010. Extended binding site on fibronectin for
1283 the functional upstream domain of protein F1 of Streptococcus pyogenes. *J Biol Chem*.
1284 285:41087-41099.

1285 Mautner, V., and R.O. Hynes. 1977. Surface distribution of LETS protein in relation to the
1286 cytoskeleton of normal and transformed cells. *J Cell Biol*. 75:743-768.

1287 McKeown-Longo, P.J., and D.F. Mosher. 1983. Binding of plasma fibronectin to cell layers of
1288 human skin fibroblasts. *J Cell Biol*. 97:466-472.

1289 Morla, A., Z. Zhang, and E. Ruoslahti. 1994. Superfibronectin is a functionally distinct form of
1290 fibronectin. *Nature*. 367:193-196.

1291 Mund, M., and J. Ries. 2020. How good are my data? Reference standards in superresolution
1292 microscopy. *Mol Biol Cell*. 31:2093-2096.

1293 Muzumdar, M.D., B. Tasic, K. Miyamichi, L. Li, and L. Luo. 2007. A global double-fluorescent
1294 Cre reporter mouse. *Genesis*. 45:593-605.

1295 Nieuwenhuizen, R.P., K.A. Lidke, M. Bates, D.L. Puig, D. Grunwald, S. Stallinga, and B.
1296 Rieger. 2013. Measuring image resolution in optical nanoscopy. *Nat Methods*. 10:557-562.

1297 Ohashi, T., D.P. Kiehart, and H.P. Erickson. 1999. Dynamics and elasticity of the fibronectin
1298 matrix in living cell culture visualized by fibronectin-green fluorescent protein. *Proc Natl Acad*
1299 *Sci U S A*. 96:2153-2158.

1300 Ovesny, M., P. Krizek, J. Borkovec, Z. Svindrych, and G.M. Hagen. 2014. ThunderSTORM: a
1301 comprehensive ImageJ plug-in for PALM and STORM data analysis and super-resolution
1302 imaging. *Bioinformatics*. 30:2389-2390.

1303 Pankov, R., E. Cukierman, B.Z. Katz, K. Matsumoto, D.C. Lin, S. Lin, C. Hahn, and K.M.
1304 Yamada. 2000. Integrin dynamics and matrix assembly: tensin-dependent translocation of
1305 alpha(5)beta(1) integrins promotes early fibronectin fibrillogenesis. *J Cell Biol*. 148:1075-1090.

1306 Pankov, R., A. Momchilova, N. Stefanova, and K.M. Yamada. 2019. Characterization of stitch
1307 adhesions: Fibronectin-containing cell-cell contacts formed by fibroblasts. *Exp Cell Res*.
1308 384:111616.

1309 Patla, I., T. Volberg, N. Elad, V. Hirschfeld-Warneken, C. Grashoff, R. Fassler, J.P. Spatz, B.
1310 Geiger, and O. Medalia. 2010. Dissecting the molecular architecture of integrin adhesion sites
1311 by cryo-electron tomography. *Nat Cell Biol*. 12:909-915.

1312 Perez, A.R., Y. Pritykin, J.A. Vidigal, S. Chhangawala, L. Zamparo, C.S. Leslie, and A.
1313 Ventura. 2017. GuideScan software for improved single and paired CRISPR guide RNA
1314 design. *Nat Biotechnol*. 35:347-349.

1315 Peters, D.M., L.M. Portz, J. Fullenwider, and D.F. Mosher. 1990. Co-assembly of plasma and
1316 cellular fibronectins into fibrils in human fibroblast cultures. *J Cell Biol*. 111:249-256.

1317 Peters, J.H., and R.O. Hynes. 1996. Fibronectin isoform distribution in the mouse. I. The
1318 alternatively spliced EIIIB, EIIIA, and V segments show widespread codistribution in the
1319 developing mouse embryo. *Cell Adhes Commun*. 4:103-125.

1320 Pliatsika, V., and I. Rigoutsos. 2015. "Off-Spotter": very fast and exhaustive enumeration of
1321 genomic lookalikes for designing CRISPR/Cas guide RNAs. *Biol Direct*. 10:4.

1322 Raitman, I., M.L. Huang, S.A. Williams, B. Friedman, K. Godula, and J.E. Schwarzbauer. 2018.
1323 Heparin-fibronectin interactions in the development of extracellular matrix insolubility. *Matrix*
1324 *Biol*. 67:107-122.

1325 Ramirez, A., and S. Astrof. 2020. Visualization and Analysis of Pharyngeal Arch Arteries using
1326 Whole-mount Immunohistochemistry and 3D Reconstruction. *J. Vis. Exp.* 157:e60797.

1327 Ran, F.A., P.D. Hsu, J. Wright, V. Agarwala, D.A. Scott, and F. Zhang. 2013. Genome
1328 engineering using the CRISPR-Cas9 system. *Nat Protoc*. 8:2281-2308.

1329 Rickelt, S., and R.O. Hynes. 2018. Antibodies and methods for immunohistochemistry of
1330 extracellular matrix proteins. *Matrix Biol*. 71-72:10-27.

1331 Ries, J. 2020. SMAP: a modular super-resolution microscopy analysis platform for SMLM data.
1332 *Nat Methods*. 17:870-872.

1333 Rozario, T., B. Dzamba, G.F. Weber, L.A. Davidson, and D.W. DeSimone. 2009. The physical
1334 state of fibronectin matrix differentially regulates morphogenetic movements in vivo. *Dev Biol*.
1335 327:386-398.

1336 Rust, M.J., M. Bates, and X. Zhuang. 2006. Sub-diffraction-limit imaging by stochastic optical
1337 reconstruction microscopy (STORM). *Nat Methods*. 3:793-795.

1338 Saitta, A.M., P.D. Soper, E. Wasserman, and M.L. Klein. 1999. Influence of a knot on the
1339 strength of a polymer strand. *Nature*. 399:46-48.

1340 Sakai, T., K.J. Johnson, M. Murozono, K. Sakai, M.A. Magnuson, T. Wieloch, T. Cronberg, A.
1341 Isshiki, H.P. Erickson, and R. Fassler. 2001. Plasma fibronectin supports neuronal survival and
1342 reduces brain injury following transient focal cerebral ischemia but is not essential for skin-
1343 wound healing and hemostasis. *Nat Med*. 7:324-330.

1344 Saunders, J.T., and J.E. Schwarzbauer. 2019. Fibronectin matrix as a scaffold for procollagen
1345 proteinase binding and collagen processing. *Mol Biol Cell*. 30:2218-2226.

1346 Schwarzbauer, J.E. 1991. Identification of the fibronectin sequences required for assembly of a
1347 fibrillar matrix. *J Cell Biol*. 113:1463-1473.

1348 Schwarzbauer, J.E., and D.W. DeSimone. 2011. Fibronectins, their fibrillogenesis, and in vivo
1349 functions. *Cold Spring Harbor perspectives in biology*. 3.

1350 Sechler, J.L., H. Rao, A.M. Cumiskey, I. Vega-Colon, M.S. Smith, T. Murata, and J.E.
1351 Schwarzbauer. 2001. A novel fibronectin binding site required for fibronectin fibril growth
1352 during matrix assembly. *J Cell Biol*. 154:1081-1088.

1353 Sechler, J.L., Y. Takada, and J.E. Schwarzbauer. 1996. Altered rate of fibronectin matrix
1354 assembly by deletion of the first type III repeats. *J Cell Biol*. 134:573-583.

1355 Shaner, N.C., P.A. Steinbach, and R.Y. Tsien. 2005. A guide to choosing fluorescent proteins.
1356 *Nat Methods*. 2:905-909.

1357 Singh, P., C. Carraher, and J.E. Schwarzbauer. 2010. Assembly of fibronectin extracellular
1358 matrix. *Annu Rev Cell Dev Biol*. 26:397-419.

1359 Singh, P., and J.E. Schwarzbauer. 2014. Fibronectin matrix assembly is essential for cell
1360 condensation during chondrogenesis. *J Cell Sci*. 127:4420-4428.

1361 Sivakumar, P., A. Czirok, B.J. Rongish, V.P. Divakara, Y.P. Wang, and S.L. Dallas. 2006. New
1362 insights into extracellular matrix assembly and reorganization from dynamic imaging of
1363 extracellular matrix proteins in living osteoblasts. *J Cell Sci*. 119:1350-1360.

1364 Skorstengaard, K., M.S. Jensen, P. Sahl, T.E. Petersen, and S. Magnusson. 1986. Complete
1365 primary structure of bovine plasma fibronectin. *Eur J Biochem*. 161:441-453.

1366 Smith, M.L., D. Gourdon, W.C. Little, K.E. Kubow, R.A. Eguiluz, S. Luna-Morris, and V. Vogel.
1367 2007. Force-induced unfolding of fibronectin in the extracellular matrix of living cells. *PLoS*
1368 *Biol*. 5:e268.

1369 Snitkovsky, S., and J.A. Young. 1998. Cell-specific viral targeting mediated by a soluble
1370 retroviral receptor-ligand fusion protein. *Proc Natl Acad Sci U S A*. 95:7063-7068.

1371 Sottile, J., and J. Chandler. 2005. Fibronectin matrix turnover occurs through a caveolin-1-
1372 dependent process. *Mol Biol Cell*. 16:757-768.

1373 Thevathasan, J.V., M. Kahnwald, K. Cieslinski, P. Hoess, S.K. Peneti, M. Reitberger, D. Heid,
1374 K.C. Kasuba, S.J. Hoerner, Y. Li, Y.L. Wu, M. Mund, U. Matti, P.M. Pereira, R. Henriques, B.
1375 Nijmeijer, M. Kueblbeck, V.J. Sabinina, J. Ellenberg, and J. Ries. 2019. Nuclear pores as
1376 versatile reference standards for quantitative superresolution microscopy. *Nat Methods*.
1377 16:1045-1053.

1378 Tomasini-Johansson, B.R., D.S. Annis, and D.F. Mosher. 2006. The N-terminal 70-kDa
1379 fragment of fibronectin binds to cell surface fibronectin assembly sites in the absence of intact
1380 fibronectin. *Matrix Biol*. 25:282-293.

1381 Tomasini-Johansson, B.R., N.R. Kaufman, M.G. Ensenberger, V. Ozeri, E. Hanski, and D.F.
1382 Mosher. 2001. A 49-residue peptide from adhesin F1 of Streptococcus pyogenes inhibits
1383 fibronectin matrix assembly. *J Biol Chem*. 276:23430-23439.

1384 von Appen, A., J. Kosinski, L. Sparks, A. Ori, A.L. DiGuilio, B. Vollmer, M.T. Mackmull, N.
1385 Banterle, L. Parca, P. Kastritis, K. Buczak, S. Mosalaganti, W. Hagen, A. Andres-Pons, E.A.
1386 Lemke, P. Bork, W. Antonin, J.S. Glavy, K.H. Bui, and M. Beck. 2015. In situ structural
1387 analysis of the human nuclear pore complex. *Nature*. 526:140-143.

1388 Wagner, D.D., and R.O. Hynes. 1979. Domain structure of fibronectin and its relation to
1389 function. Disulfides and sulfhydryl groups. *J Biol Chem*. 254:6746-6754.

1390 Wierzbicka-Patynowski, I., Y. Mao, and J.E. Schwarzbauer. 2004. Analysis of fibronectin
1391 matrix assembly. *Current protocols in cell biology / editorial board, Juan S. Bonifacino ... [et*
1392 *al.]*. Chapter 10:Unit 10 12.

1393 Wijelath, E.S., J. Murray, S. Rahman, Y. Patel, A. Ishida, K. Strand, S. Aziz, C. Cardona, W.P.
1394 Hammond, G.F. Savidge, S. Rafii, and M. Sobel. 2002. Novel Vascular Endothelial Growth
1395 Factor Binding Domains of Fibronectin Enhance Vascular Endothelial Growth Factor Biological
1396 Activity. *Circulation research*. 91:25-31.

1397 Zamir, E., B.Z. Katz, S. Aota, K.M. Yamada, B. Geiger, and Z. Kam. 1999. Molecular diversity
1398 of cell-matrix adhesions. *J Cell Sci*. 112 (Pt 11):1655-1669.

1399 Zamir, E., M. Katz, Y. Posen, N. Erez, K.M. Yamada, B.Z. Katz, S. Lin, D.C. Lin, A.
1400 Bershadsky, Z. Kam, and B. Geiger. 2000. Dynamics and segregation of cell-matrix adhesions
1401 in cultured fibroblasts. *Nat Cell Biol*. 2:191-196.

1402 Zhang, Q., W.J. Checovich, D.M. Peters, R.M. Albrecht, and D.F. Mosher. 1994. Modulation of
1403 cell surface fibronectin assembly sites by lysophosphatidic acid. *J Cell Biol*. 127:1447-1459.

1404 Zhang, Q., M.K. Magnusson, and D.F. Mosher. 1997. Lysophosphatidic acid and microtubule-
1405 destabilizing agents stimulate fibronectin matrix assembly through Rho-dependent actin stress
1406 fiber formation and cell contraction. *Mol Biol Cell*. 8:1415-1425.

1407 Zhang, Q., and D.F. Mosher. 1996. Cross-linking of the NH2-terminal region of fibronectin to
1408 molecules of large apparent molecular mass. Characterization of fibronectin assembly sites
1409 induced by the treatment of fibroblasts with lysophosphatidic acid. *J Biol Chem*. 271:33284-
1410 33292.

1411 Zhong, C., M. Chrzanowska-Wodnicka, J. Brown, A. Shaub, A.M. Belkin, and K. Burridge.
1412 1998. Rho-mediated contractility exposes a cryptic site in fibronectin and induces fibronectin
1413 matrix assembly. *J Cell Biol*. 141:539-551.

1414 Zhou, X., R.G. Rowe, N. Hiraoka, J.P. George, D. Wirtz, D.F. Mosher, I. Virtanen, M.A.
1415 Chernousov, and S.J. Weiss. 2008. Fibronectin fibrillogenesis regulates three-dimensional
1416 neovessel formation. *Genes Dev*. 22:1231-1243.
1417

Table 1

Sample	Buffer	ELE (%)	Average # Localizations per NPC	# Localizations per protein	Radius of NPC, nm
U2OS-Nup96	GLOX/BME	79.6+/-5.4	280 +/- 49.2	8.75 +/- 1.54	63.6 +/- 0.86

NUP96$^{mEGFP/mEGFP}$ cells were imaged using αGFP 1° antibody and AF647-conjugated 2° antibody detecting NUP96-mEGFP; Data is from 3 independent experiments, eight cells, and 4571 NPCs

Table 2

	Buffer	Average PSF (nm)	Average # Localizations per nanodomain	Median Localization Precision, nm	# of mEGFP molecules per nanodomain in Fn1-GFP fibrils	Diameter of Fn1 nanodomain, nm	Nanodomain periodicity, nm
$Fn1^{mEGFP/mEGFP}$ MEFs; αGFP 1° antibody; AF647-conjugated 2° antibody	GLOX/BME	143.8 +/- 2.35	159 +/- 77.92	9.1 +/- 1.9	16.85 +/- 5.1	28.26+/-9.7	102±29

αGFP 1° antibody; AF647-conjugated 2° antibody were used to detect Fn1-mEGFP. Data is from 3 independent experiments, 6 cells, 52 fibrils and 833 nanodomains were used to calculate the number of GFP molecules per nanodomain
Data from 3 independent experiments, 15 cells, 27 fibrils, and 1292 nanodomains were used to quantify nanodomain diameter

Figure 1

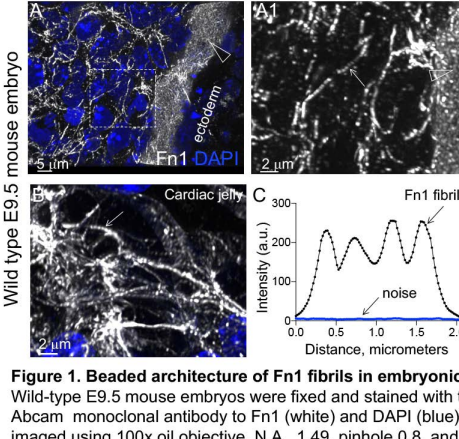

Figure 1. Beaded architecture of Fn1 fibrils in embryonic ECM. Wild-type E9.5 mouse embryos were fixed and stained with the Abcam monoclonal antibody to Fn1 (white) and DAPI (blue), and imaged using 100x oil objective, N.A. 1.49, pinhole 0.8, and sampling rate of 40 nm/pixel. **A – A1.** Sagittal optical section through the first pharyngeal arch and **B.** the cardiac jelly, an ECM-rich region between the myocardial and endocardial layers of the cardiac outflow tract. Large arrowheads in **A – A1** point to the ECM at the ectoderm-mesenchyme boundary of the 1st pharyngeal arch. The box in **(A)** is expanded in **A1** to show Fn1 microarchitecture. Arrow in **A1** points to a beaded Fn1 fibril within the 1st arch mesenchyme; **B.** Beaded architecture of Fn1 fibrils in cardiac jelly, e.g., arrow. **C.** Intensity profile plot of a Fn1 fibril shows a regularly-undulating profile, with troughs well above the noise; a.u. arbitrary units.

Figure 2

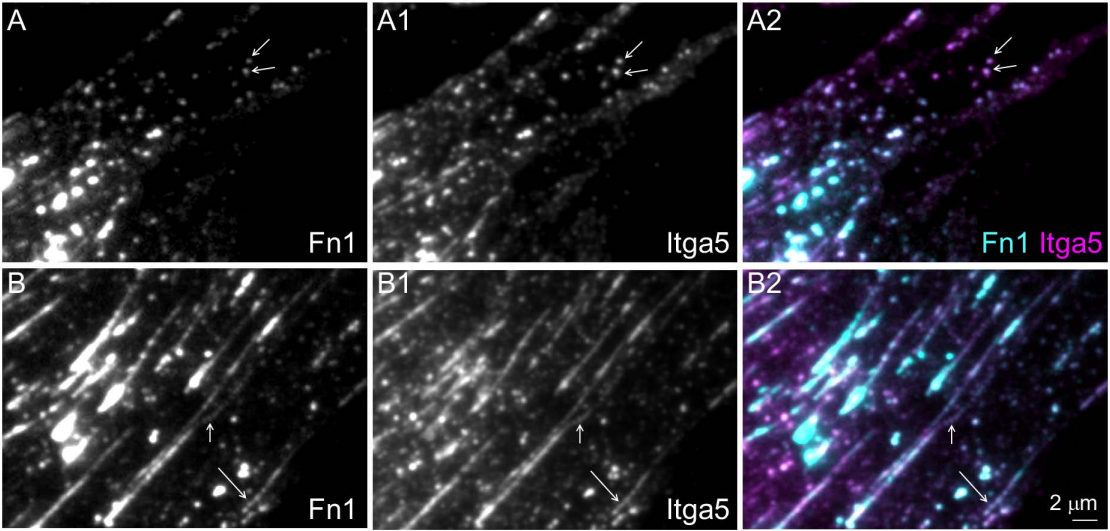

Figure 2. Integrin α5 and Fn1 co-localize in beaded adhesions. Wild-type MEFs were plated for 16 hours on glass coverslips without coating, then fixed, stained with Abcam monoclonal antibodies to Fn1 and anti-integrin α5 (Itga5) antibodies. Cells were imaged at the critical angle of incidence using 100x oil objective, NA 1.49. **A – A2** cell periphery. Arrows in **A-A2** point to examples of non-fibrillar Fn1 adhesions. **B – B2** medial portion of a cell containing beaded fibrillar adhesions (arrows). Magnifications in all panels are the same.

Figure 3

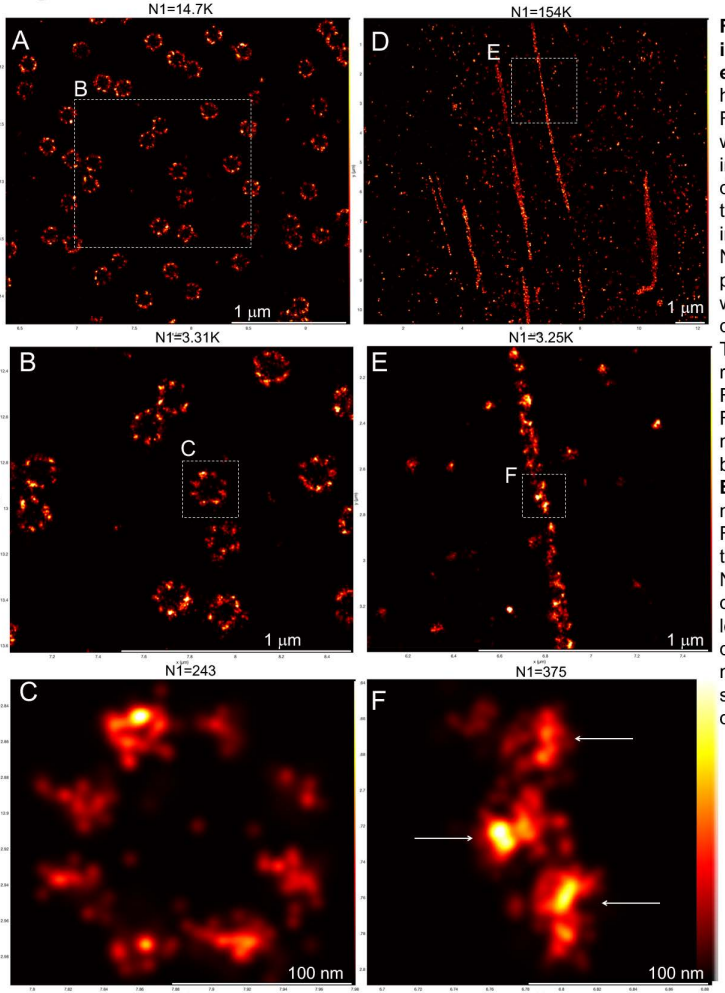

Figure 3. Standardized SMLM imaging results in high resolution and high effective labeling efficiency (ELE). NUP96$^{mEGFP/mEGFP}$ homozygous knock-in cells (**A-C**) and Fn1$^{mEGFP/mEGFP}$ homozygous knock-in cells (**D-F**) were imaged using the same staining and imaging solutions containing anti-GFP 1° at 1:100 dilution and Alexa-647-conjugated 2° antibodies, the same GLOX/BME buffer, and the same imaging protocol (*see Methods*). **A-C.** NUP96$^{mEGFP/mEGFP}$ cells. The majority of nuclear pore complexes (NPCs) show 8-fold symmetry with 8 corners labeled by NUP96. See *Table 1* for quantification of NPC dimensions and the ELE. The resolution in (**C**) measured by the Fourier ring curve method is 18.3+/-6.7 nm. **D-F.** Fn1$^{mEGFP/mEGFP}$ cells. Nanodomain architecture of Fn1-mEGFP fibrils is clearly visible in subsequent magnifications of the fibril boxed in (**D**). The boxed region in **D** is shown in **E**. Boxed region in **E** is shown in **F**. Arrows in **F** point to Fn1 nanodomains. The resolution in (**F**) measured by Fourier ring curve method is 14.5+/-1.1 nm. Note that nanodomain size is similar to the size of an NUP96+ NPC corner, which is ~12 nm in actual diameter. N1 is the number of grouped localizations in each panel. See *Table 2* for quantifications of the numbers of mEGFP molecules per nanodomain. Vertical bar in **F** shows color-coding according to localization density for all panels in this figure.

Figure 4

A Schematic of Fn1 dimer

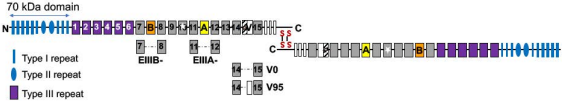

B Antibodies used in these studies and their epitopes

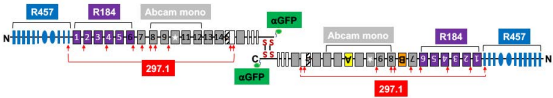

Figure 4. Schematic representations of Fn1 dimers and antibody binding sites. A. Fn1 is secreted as a dimer. Two di-sulfide bonds at the C-terminus hold Fn1 molecules in an anti-parallel orientation. 70 kDA Fn1 assembly domain is marked in blue and by a double-headed arrow. Fn1 type III repeats are numbered. Splice variants characterized in mice are shown. **B.** Schematic of binding sites for the antibodies used in this manuscript. All antibodies except one are polyclonal, see *Table M2* in the Methods section. R457 is a rabbit polyclonal antibody raised to the 70 kDA domain of Fn1; R184 is a rabbit polyclonal raised against the first six type III repeats (purple); 297.1 is a rabbit polyclonal antibody raised to the full length rat plasma Fn1; The binding sites of 297.1 (red arrows) were mapped in this study (see **Sup. Fig. 4**); Abcam mono is a monoclonal antibody recognizing an epitope within the marked region. αGFP is a polyclonal antibody raised to GFP.

Figure 5

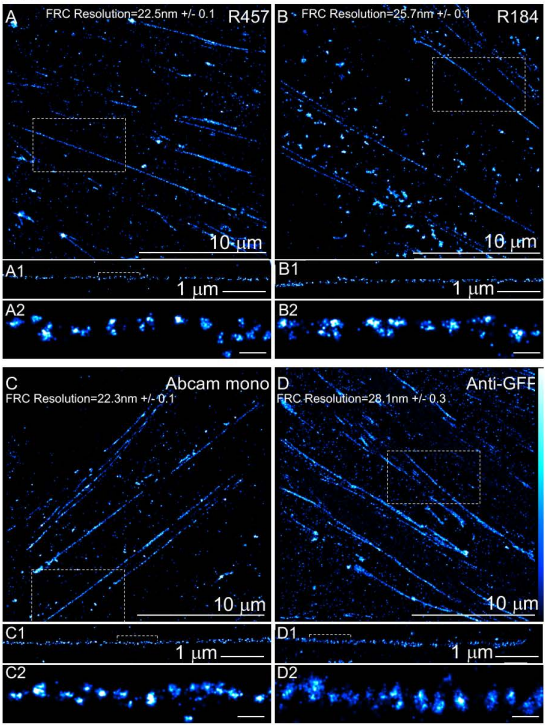

Figure 5. Nanodomain architecture of Fn1 fibrils detected with four different antibodies. Fn1$^{mEGFP/mEGFP}$ MEFs were plated on glass cover slips without coating, cultured over night, and stained with the following antibodies: **A.** R457 (1:200 dilution). **B**. R184 (1:100 dilution). **C**. Abcam monoclonal antibody (1:200 dilution). **D**. anti-GFP antibody (1:100 dilution). Boxes in **A, B, C,** and **D** are expanded to show fibrils in **A1, B1, C1**, and **D1**, respectively. Brackets in **A1, B1, C1,** and **D1** are expanded in **A2, B2, C2**, and **D2**, respectively. Scale bars in **A2, B2, C2**, and **D2** are 100 nm. Fourier ring correlation (FRC) was used to determine image resolution. Vertical bar in **D** shows color-coding according to localization density for all panels in this figure.

Figure 6

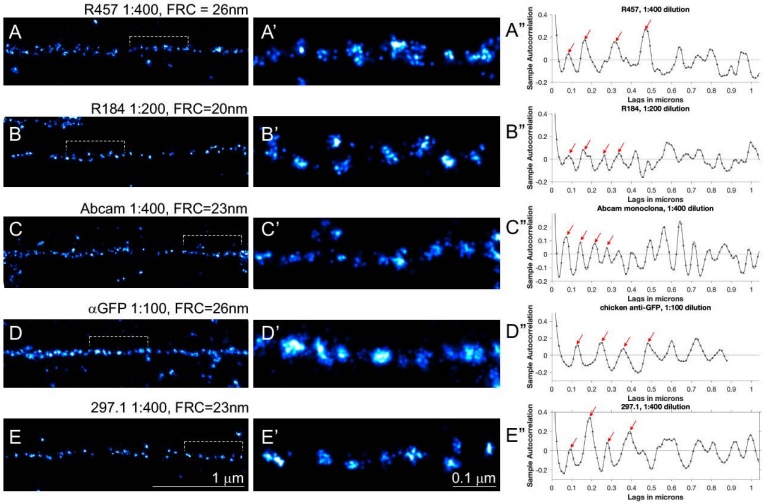

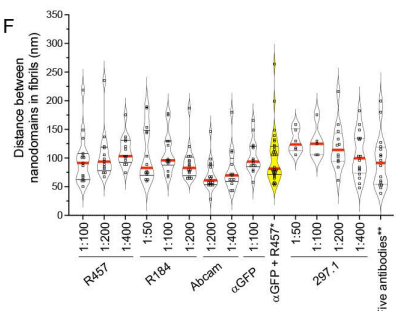

Figure 6. Periodical labeling of Fn1 fibrils by multiple antibodies, their dilutions and combinations. Fn1$^{mEGFP/mEGFP}$ MEFs were plated on glass cover slips without coating, cultured over night, and stained with antibodies indicated. **A-E.** SMLM images resulting from the highest dilutions of antibodies tested. Brackets in **A – E** are expanded in **A'-E'. A''-E''** Autocorrelation traces for fibrils shown in **A-E.** Ljung-Box Q-test for autocorrelation at the peak positions marked by the red arrows resulted in h=1, p=0 indicating strong evidence of autocorrelation at least up to the 4th peak; h (the null hypothesis for this test) is that the first 4 autocorrelations are jointly zero. $h=1$ rejects this hypothesis. **F.** Summary of autocorrelation analyses of multiple fibrils (each fibrils analyzed is marked by a square) stained with different antibody dilutions, and combinations of antibodies. Experiments for each antibody dilution were repeated three independent times, and each time, at least three cells were imaged. One-way ANOVA test with Tukey's correction for multiple testing showed no significant differences among the means. * αGFP and R457 were both used at 1:100 dilution. ** The 5 antibodies used and their dilutions were the following: R457(1:400), R184(1:200), Abcam (1:400), αGFP (1:100), 297.1(1:400).

Figure 7

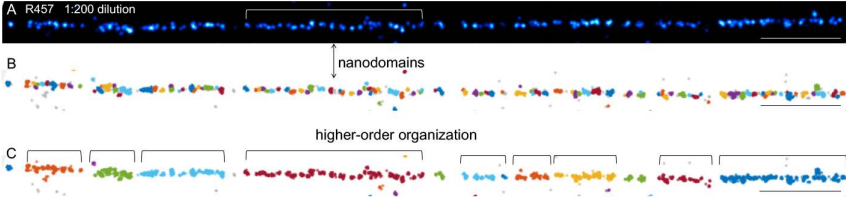

Figure 7. Clustering using DBSCAN suggests a higher-order organization of Fn1 nanodomains in fibrils. Fn1$^{mEGFP/mEGFP}$ MEFs were plated on glass cover slips without coating, cultured over night, and stained with antibody indicated. The fibril in **A** was analyzed by DBSCAN clustering in **B** and **C**. The minimum number of points per neighborhood (k) was set to 4, as recommended for all 2-dimentional datasets. **B.** The size of the neighborhood, ε, was set to 14 nm an apparent average radius of Fn1 nanodomain (*Table 2*). Adjacent clusters are labeled with different colors. **C**. ε was estimated automatically by the DBSCAN algorithm. Localizations in the same cluster are given the same color; Adjacent clusters are labeled with different colors. DBSCAN clustering in **A** using ε=14 nm discovers Fn1 nanodomains (compare SMLM image above). Clustering in **C** using an unbiased estimate of ε suggests a higher-order organization of Fn1 nanodomains. Scale bar is 1 micron.

Figure 8

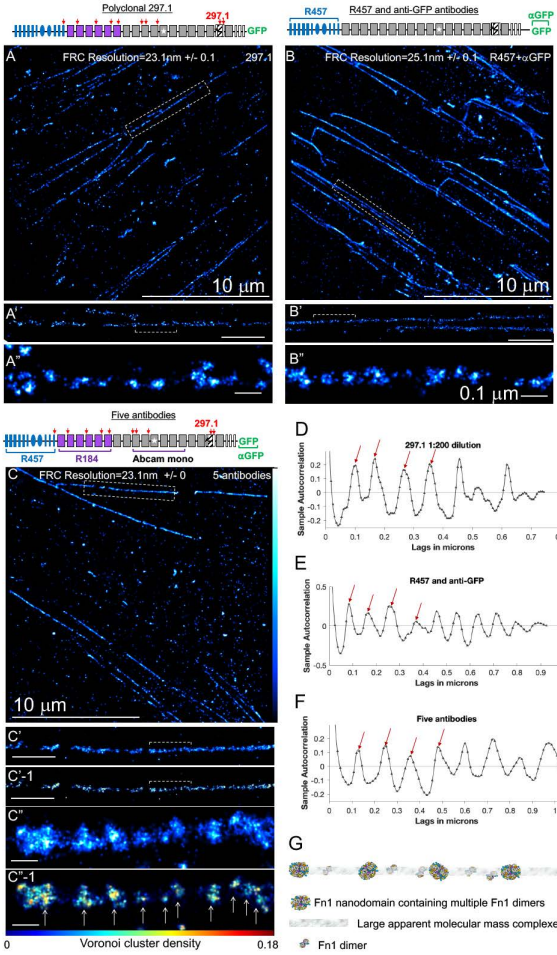

Figure 8 Polyclonal antibody to full-length Fn1 and combinations of antibodies recognizing epitopes along the length of Fn1 reveal periodical nanodomain architecture of Fn1 fibrils. $Fn1^{mEGFP/mEGFP}$ MEFs were plated on glass cover slips without coating, cultured over night, and stained with the indicated antibodies.

A. 297.1 rabbit polyclonal antibody raised to full-length, plasma Fn1 recognizing multiple epitopes along Fn1 molecule (red arrows), 1:200 dilution. **B.** A combination of anti-GFP antibody (1:100) and R457 antibody (1:100). **C.** Staining using a combination of 5 antibodies depicted in a schematic above the panel. For dilutions of 5 antibodies see legend to *Fig. 6F*.

Boxed fibrils in **A, B, C** are expanded in **A', B', C'** and **C'-1** (scale bars in **A',B',C',** and **C'-1** are 1 µm). Bracketed regions in **A', B', C'** are expanded in **A", B", C"** and **C'-1** (scale bars in **A", B", C"** and **C"-1** are 0.1 µm). **C'-1** and **C"-1**. The Voronoi tessellation method assigns localization densities to clusters corresponding with nanodomains (arrows in **C"-1**).

Vertical bar in **C** shows color-coding according to localization density for all panels in this figure, except **C'-1** and **C"-1**. **C'-1** and **C"-1** are color-coded according to Voronoi cluster density (horizontal bar below **C"-1**). **D – F.** Autocorrelation analysis and Ljung-Box Q-test for autocorrelation at the peak positions marked by the red arrows resulted in $h=1$, $p=0$ indicating strong evidence of autocorrelation at least up to the 4th peak; h (the null hypothesis for this test) is that the first 4 autocorrelations are jointly zero. $h=1$ rejects this hypothesis. **G.** A model of Fn1 fibril. In this model Fn1 fibrils are composed of periodically-spaced nanodomains containing multiple Fn1 dimers. Nanodomains may be linked via large molecular mass complexes (LAMMs, Zhang and Mosher, 1996) with a few Fn1 dimers between the nanodomains. For additional/alternative models see *Discussion* and *Sup. Fig. 8F1-F2.*

Figure 9

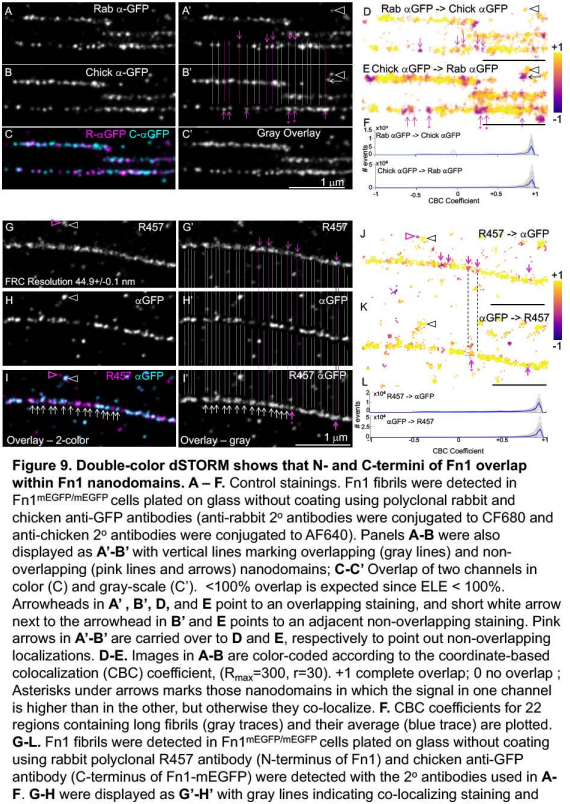

Figure 9. Double-color dSTORM shows that N- and C-termini of Fn1 overlap within Fn1 nanodomains. A – F. Control stainings. Fn1 fibrils were detected in $Fn1^{mEGFP/mEGFP}$ cells plated on glass without coating using polyclonal rabbit and chicken anti-GFP antibodies (anti-rabbit 2º antibodies were conjugated to CF680 and anti-chicken 2º antibodies were conjugated to AF640). Panels **A-B** were also displayed as **A'-B'** with vertical lines marking overlapping (gray lines) and non-overlapping (pink lines and arrows) nanodomains; **C-C'** Overlap of two channels in color (C) and gray-scale (C'). <100% overlap is expected since ELE < 100%. Arrowheads in **A' , B', D,** and **E** point to an overlapping staining, and short white arrow next to the arrowhead in **B'** and **E** points to an adjacent non-overlapping staining. Pink arrows in **A'-B'** are carried over to **D** and **E**, respectively to point out non-overlapping localizations. **D-E.** Images in **A-B** are color-coded according to the coordinate-based colocalization (CBC) coefficient, (R_{max}=300, r=30). +1 complete overlap; 0 no overlap ; Asterisks under arrows marks those nanodomains in which the signal in one channel is higher than in the other, but otherwise they co-localize. **F.** CBC coefficients for 22 regions containing long fibrils (gray traces) and their average (blue trace) are plotted. **G-L.** Fn1 fibrils were detected in $Fn1^{mEGFP/mEGFP}$ cells plated on glass without coating using rabbit polyclonal R457 antibody (N-terminus of Fn1) and chicken anti-GFP antibody (C-terminus of Fn1-mEGFP) were detected with the 2º antibodies used in **A-F**. **G-H** were displayed as **G'-H'** with gray lines indicating co-localizing staining and pink lines pointing at non-colocalizing staining. **I - I'** show merged signals for the two antibodies in color (**I**) and gray scale (**I'**). Arrows in **I-I'** point to nanodomains. White and pink arrowheads in **G-I** also show overlapping and non-overlapping nanodomain staining, respectively, as seen in **J-K**. **J-K.** Images in **G-H** are color-coded according to the coordinate-based colocalization (CBC) coefficient, (R_{max}=300, r=30). Pink arrows in **G'-H'** correspond with pink arrows in **J-K,** respectively. Asterisk under the arrow marks the nanodomains in which the signal in **H'** is higher than in **G'**, but otherwise they co-localize. Note that the settings for the CBC analysis distinguish overlapping and non-overlapping localizations in adjacent nanodomains. **L**. CBC coefficients for 20 regions containing long fibrils (gray traces) and their average (blue trace) are plotted, showing a high probability of a near complete overlap between the N- and C- termini. All scale bars are 1 µm.

Figure 10

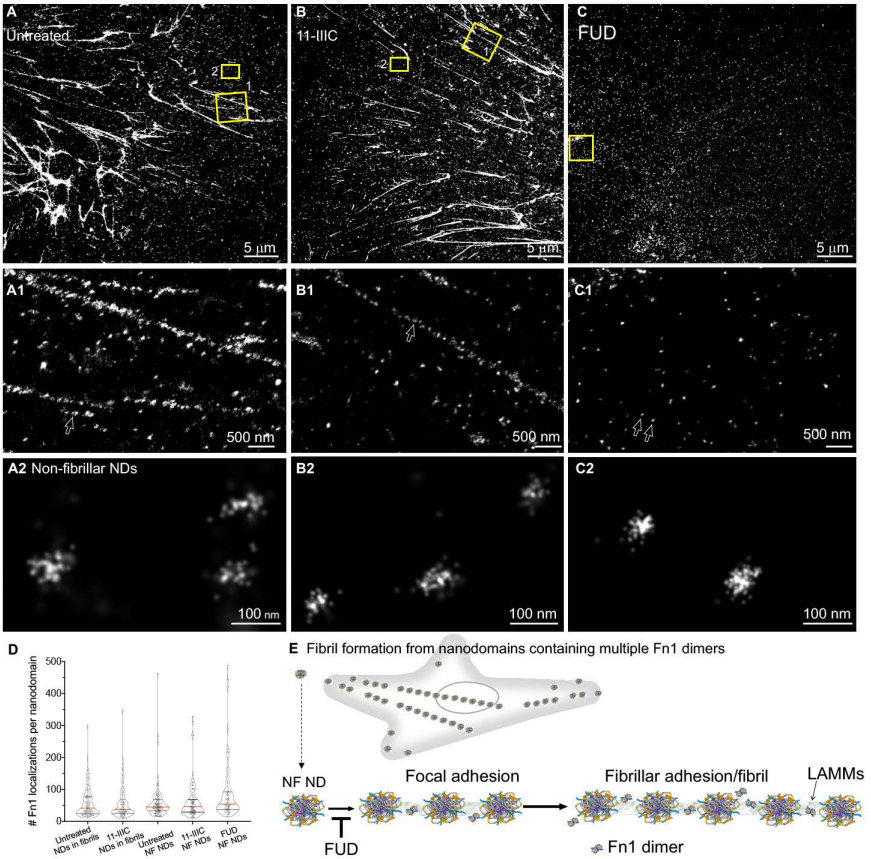

Figure 10. The N-terminal Fn1 assembly domain regulates the organization of Fn1 nanodomains into linear fibrillar arrays. Fn1$^{mEGFP/+}$ MEFs were plated on glass and were either left untreated (**A-A2**), incubated with the control 11-IIIC peptide (**B-B2**), or the FUD peptide (**C-C2**) for 16 hrs. Cells were then washed with PBS, fixed and stained with the Abcam monoclonal antibody to Fn1 followed by Alexa 647-conjugated secondary antibodies. Cells were imaged at the critical angle of incidence by dSTORM. **A – A2**. Untreated, non-permeabilized cells. **B – B2.** Cells incubated with control 11-IIIC peptide, non-permeabilized. **C – C2.** FUD-treated, non-permeabilized cells. Boxes marked 1 in **A-B** are expanded in **A1-B1**. Boxes marked 2 in **A-B**, are expanded in **A2 – B2**. The box in **C** is expanded in **C1** and **C2**. Arrows in **A1-B1** point to Fn1 nanodomains (NDs) in fibrils. Arrows in **C1** points to non-fibrillar (NF) nanodomains expanded in **C2**; **D.** Quantification of the number of grouped Fn1 localizations in nanodomains in fibrils and in non-fibrillar nanodomains after various conditions. Red lines mark medians. Differences are not statistically significant, Kruskal-Wallis test with Dunn's correction for multiple testing. **E.** Model of fibril formation: 6-11 Fn1 dimers assemble into nanodomains containing integrin $\alpha5\beta1$ at cell periphery, move rearward with actin flow, and become organized into linear arrays of nanodomains. Joining of the additional Fn1 nanodomains to these arrays leads to the generation of longer fibrils as assemblies move toward the cell center. FUD does not interfere with the formation of Fn1 nanodomains; Instead, it blocks the organization of Fn1 nanodomains into linear arrays. LAMMs – large apparent molecular mass complexes, defined in Zhang et al., 1996.